The Design of MnOx Based Catalyst in Post-Plasma Catalysis Configuration for Toluene Abatement

Zhiping Ye, Jean-Marc Giraudon, Nathalie de Geyter, Rino Morent, Jean-Francois Lamonier

catalysts

MDPI

Review

The Design of MnO_x Based Catalyst in Post-Plasma Catalysis Configuration for Toluene Abatement

Zhiping Ye [1,2], Jean-Marc Giraudon [1,*], Nathalie De Geyter [2], Rino Morent [2] and Jean-François Lamonier [1]

[1] Univ. Lille, CNRS, Centrale Lille, ENSCL, Univ. Artois, UMR 8181—UCCS—Unité de Catalyse et Chimie du Solide, F-59000 Lille, France; yzp8237610@gmail.com (Z.Y.); jean-francois.lamonier@univ-lille1.fr (J.-F.L.)

[2] Research Unit Plasma Technology, Department of Applied Physics, Faculty of Engineering and Architecture, Ghent University, Sint-Pietersnieuwstraat 41, 9000 Ghent, Belgium; Nathalie.DeGeyter@UGent.be (N.D.G.); Rino.Morent@ugent.be (R.M.)

* Correspondence: jean-marc.giraudon@univ-lille1.fr; Tel.: +33-320436856

Received: 21 December 2017; Accepted: 11 February 2018; Published: 23 February 2018

Abstract: This review provides an overview of our present state of knowledge using manganese oxide (MnO_x)-based catalysts for toluene abatement in PPC (Post plasma-catalysis) configuration. The context of this study is concisely sum-up. After briefly screening the main depollution methods, the principles of PPC are exposed based on the coupling of two mature technologies such as NTP (Non thermal plasma) and catalysis. In that respect, the presentation of the abundant manganese oxides will be firstly given. Then in a second step the main features of MnO_x allowing better performances in the reactions expected to occur in the abatement of toluene in PPC process are reviewed including ozone decomposition, toluene ozonation, CO oxidation and toluene total oxidation. Finally, in a last part the current status of the applications of PPC using MnO_x on toluene abatement are discussed. In a first step, the selected variables of the hybrid process related to the experimental conditions of toluene abatement in air are identified. The selected variables are those expected to play a role in the performances of PPC system towards toluene abatement. Then the descriptors linked to the performances of the hybrid process in terms of efficiency are given and the effects of the variables on the experimental outcomes (descriptors) are discussed. The review would serve as a reference guide for the optimization of the PPC process using MnO_x-based oxides for toluene abatement.

Keywords: NTP (Non thermal plasma); principles of catalyst selection; MnO_x; PPC (Post plasma-catalysis); toluene abatement; ozone decomposition ability; toluene ozonation; CO oxidation; toluene total oxidation

1. Introduction

With the increasing consumption of toluene in commercial and industrial applications [1], the toluene emission problem becomes of serious concern for causing environmental problem as well as inducing negative health effects on humans [2,3]. So it is highly desired to find an economical and green technique for toluene emission control. Comparing to traditional techniques such as high-temperature-based combustion and catalytic oxidation, non-thermal plasma (NTP) technology is capable of operating at room temperature and ambient pressure. Meanwhile, easy operation is another main advantages of NTP technique [4]. However, the energy efficiency and CO_2 selectivity still need to be improved for further industrial application. Hence, plasma-catalysis, including in plasma catalysis (IPC) and PPC configurations, can be a promising approach for toluene abatement having the advantages of higher toluene removal efficiency and lower unwanted byproducts at a low operating temperature, at which it is normally not possible to activate the catalysts [5,6].

To begin with, the physico-chemical properties of toluene are presented and its negative effects on environment and human being are given. Then, after briefly screening the most encountered VOCs (Volatile Organic Compounds) depollution methods, the principles of PPC are exposed based on the coupling of two mature technologies such as NTP and catalysis. The design of manganese oxides is discussed in a fourth part. The choice of MnO_x as potential catalysts in PPC configuration was motivated due to the fact that except metals of the platinum group, characterized by their high price, the metal oxide catalysts containing manganese oxide exhibit the highest activity in decomposition of gaseous ozone and also in catalytic oxidation of pollutants. In that respect, the presentation of the abundant manganese is firstly given. Then, the important features of MnO_x allowing better performances in the main reactions expected to occur in the abatement of toluene in a PPC process are reviewed including catalytic oxidation of toluene, ozone decomposition, toluene ozonation and CO oxidation. Finally, in a last part the current status of the applications of PPC using MnO_x-based type catalysts on toluene abatement is discussed. The selected variables of the hybrid process related to the experimental conditions of toluene abatement in air are first identified. The selected variables are those expected to play a role in the performances of the two-stage plasma-catalyst system towards toluene abatement. The descriptors linked to the performances of the hybrid process in terms of process efficiency are also presented. In a second step the effects of the variables on the experimental outcomes (descriptors) are discussed.

2. The Properties, Applications and Hazardous Effects of Toluene

Toluene ($C_6H_5CH_3$) is widely investigated as a representative VOCs of the BTX (Benzene, Toluene and Xylene) family. Toluene is a colorless liquid with an aromatic odor. It is a mono-substituted benzene derivative, consisting of a CH_3 group attached to a phenyl group. The basic properties of toluene are presented in Table 1.

Table 1. The physicochemical properties of toluene.

Property	Value
Chemical formula	C_7H_8
No. CAS	108-88-3
Molar mass (g/mol)	92.14
Density (g/mL)	0.87 (20 °C)
Melting point (°C)	−95
Boiling point (°C)	111
Solubility in water (g/L)	0.52 (20 °C)
Vapor pressure (kPa)	2.8 (20 °C)
Odor threshold (ppmv, Parts Per Million by volume)	0.17
Auto ignition temperature (°C)	480
Conversion factor	1 ppmv = 3.76 mg/m^3 (in air, 25 °C)

Toluene can react as an aromatic hydrocarbon in electrophilic aromatic substitution [7]. The methyl group has a greater electron-releasing property than that of H atom in the same position. Sulfation, chlorination and halogenation have been undergone via this property. Importantly, comparing to the phenyl group, methyl group is more susceptible to oxidation [8].

Toluene has numerous commercial and industrial applications: for example, toluene is used as a precursor in the synthesis of chemicals, such as xylene, benzene, toluene diisocyanate (TDI) for the manufacture of polyurethane foam and trinitrotoluene (the explosive TNT). Toluene is used as an octane booster in gasoline fuels, which are used in internal combustion engines. In addition, toluene is widely used as a solvent because of its favorable properties, such as high solvency, low flammability, non-corrosiveness and high stability. In many commercial products, toluene is present in paint thinners, silicone sealants, nail polish remover, glues, disinfectants and correction fluid. The global demand for toluene valued at over USD 25.1 billion in 2015, is expected to reach above USD 31.8 billion in 2021 [9].

Toluene worldwide production is estimated to be 19.6 million tons in 2020 comparing to 12.4 million in 2010 [10].

However, it is noteworthy to mention that ~86% of the toluene produced is eventually released into the biosphere (primarily in the troposphere) due to high volatility and low solubility in water. There are several man-made sources of emissions to the atmosphere, including the following [11]:

- Inadvertent sources (65%), such as emissions from motor vehicles and aircraft exhaust, losses during gasoline marketing activities, chemical spills, cigarette smoke, and household products.
- Industrial processes in which toluene is used (33%).
- Toluene production (2%).

Toluene is believed to be one of the most prevalent hydrocarbons in the troposphere. Its dispersion is largely dependent upon meteorological conditions and its atmospheric reactivity. The lifetime of toluene ranges from 4 days (at high-altitudes during the summer) to several months (at low-altitudes during the winter). The average half-life of toluene resulting from atmospheric oxidation is estimated to be 12.8 h [3]. So the contribution of toluene to the photochemical smog is considerable.

The presence of toluene in air has a negative impact on human health. Toluene is a main contributor of indoor environmental pollution. Different sources such as paints, adhesives and cigarette are known to contribute to the increase of toluene concentration in indoor air.

The report entitled "toxicological profile for toluene" published in 2000 conducted by U.S. department of health and human services presents the health effects of toluene [2]. As shown in Table 2, there are three main exposure routes for human: inhalation, oral and dermal. Among them, a lot of data deal with toluene incorporation throughout inhalation. The high hazard profile of toluene is highlighted as it covered all the possible health effects listed in Table 2. For example, in Virginia, it was reported that 39 deaths were attributed to inhalant abuse from 1987 to 1996, and Hobara et al. [12] estimated 1 h of exposure to 1800–2000 ppm toluene may be fatal to humans via inhalation. Regarding oral route, only cases of death and acute effect have been reported. Concerning the dermal route, it has been found that exposure of toluene caused the acute effect and genotoxic effect. Due to the adverse effects on human health, WHO (Word Health Organization) has published guideline for the toluene exposure limit. European Union has followed the instruction of WHO [1]: The lowest-observed-adverse-effect level on the central nervous system (CNS) from occupational studies, is approximately 332 mg/m^3 (88 ppmv) and the limit of occupational exposure for 8 h of work is 188 mg/m^3 (46 ppmv) in European Union (EU).

Table 2. Existing information on health effects of toluene (black dot: existing data); adapted from reference [2].

Health Effects	Oral	Dermal
Death	●	
Acute	●	●
Intermediate		
Chronic		
Immunologic/Lyphoretic		
Neurologic		
Reproductive		
Developmental		
Genotoxic		●
Cancer		

3. The Treatment Techniques for the Removal of Toluene

The dangerousness of toluene involves researching an economic and green technique for its abatement. There have been developing a few traditional types of VOCs abatement techniques, mainly focus on two directions: one deals with non-destructive methods (adsorption, condensation, membrane separation), the other one concerns destructive methods (biochemical method, thermal and catalytic oxidations). The limits based on VOCs concentration and flow rate for these conventional methods have been depicted in Figure 1. Since every type of treatment technology has advantages and disadvantages, none is really satisfactory.

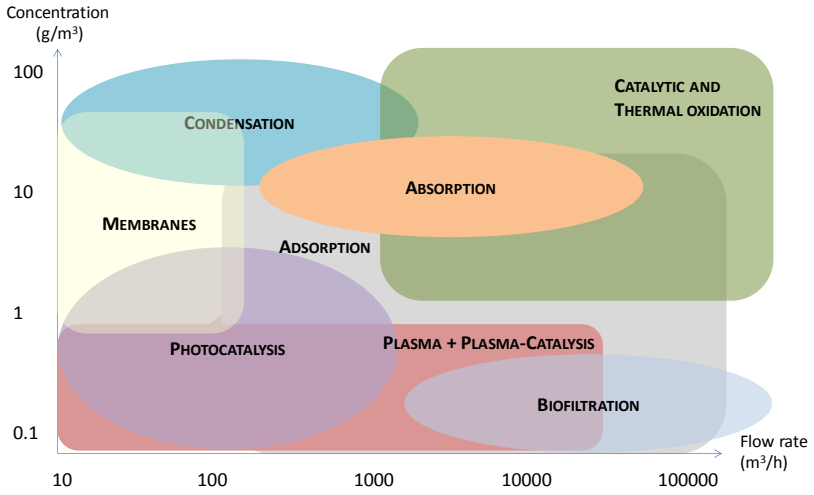

Figure 1. Classification of various air pollution control technologies based on air flow rate and initial VOC concentration.

Comparing to conventional methods, NTP technology has been claimed to be an alternative method for reducing VOCs due to its wide applicable range of 10–50,000 $Nm^3 \cdot h^{-1}$ and (ppb level)-10,000 ppmv [13–16], especially effective for concentrations lower than 100 ppmv [17]. The application of NTP on toluene abatement has attracted considerable interest because of easy on/off operation and inexpensiveness [18,19]. Generally, NTP consists of energetic electrons, ions, active radicals, neutral particles and UV photons as shown in Figure 2. These species are produced when a sufficient strong electric field was applied allowing gas discharge. The electron energy is usually considered to range from 1 to 20 eV while the temperature of the carrier gas keeps close to room temperature. These high energetic electrons can promote toluene abatement via a primary process such as charge transfer, ionization, excitation, dissociation reactions [20]. The secondary process is characterized by the subsequent chemical reactions involving the products of primary process (electrons, radicals, ions, and excited molecules). However, the overall process is not selective into the desired target which is CO_2. To overcome lack of CO_2 selectivity, researchers have focused on emerging techniques resulting from the coupling of two mature VOCs abatement technologies. Among those, plasma-catalysis is one of the most promising. Attractiveness of this hybrid process stems from the possibility to take full advantages of the two technologies: high selectivity from catalysis and the easy operation from NTP. Thus, previous works have emphasized the beneficial role of plasma-catalysis in VOCs removal allowing to decrease the energy cost as well as minimizing the production of hazardous by-products [17,21,22].

According to the location of catalyst, the plasma catalysis system can be divided into two categories, namely, IPC and PPC configurations. In this study, we will focus only on PPC applied to toluene removal.

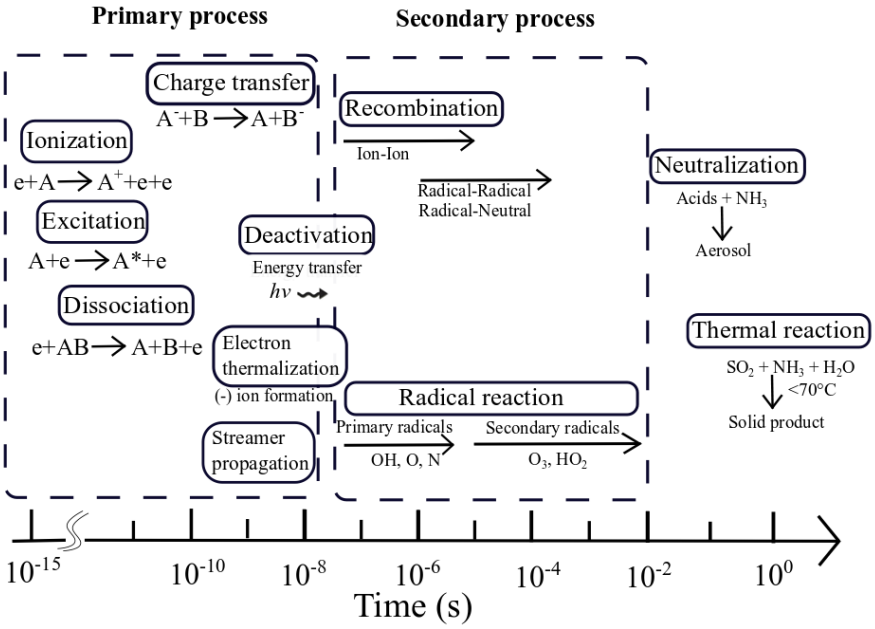

Figure 2. Time-scale of elementary processes in a non thermal process [20].

4. Design of Catalysts for Toluene Abatement in PPC Process

4.1. Introduction

In PPC configuration the catalyst is located downstream from the non-thermal plasma reactor. In that way homogeneous complex reactions occur between plasma and the carrier gas molecules such as O_2, N_2, possible H_2O and the VOC whose number and extent can be tuned by changing the energy put in the plasma. Due to the low selectivity of the NTP, along the VOC oxidation into CO_2, its transformation is always accompanied by the formation of unwanted hazardous byproducts (e.g., plasma generated VOCs (reaction intermediates), CO, O_3, and NO_x). This problem can be resolved a priori through the high selectivity of the catalyst. For instance, the proper catalyst should be able to oxidize the plasma generated organic by-products and the plasma non processed initial VOC as well as CO to CO_2 and decompose O_3 and NO_x generally in moist air at a temperature close to room temperature or moderate ($\leq$150 °C) at the same time. The basic idea is to take advantage of the O_3 decomposition efficiency of the catalyst to supply active species enabling the total oxidation of plasma non processed hazardous species. When regarding the nature of the catalysts, noble metals and transition metal oxides have been found to be the most active substances for ozone decomposition. However among the developed catalysts, MnO_x are considered to be the most efficient and cost-effective for ozone decomposition. Additionally, the possibility of increasing moderately the temperature of the catalyst allows to activate some oxygen of the catalyst. Based on that observation, efficient catalysts for total oxidation of VOC cannot be discarded. Again, the same families of catalysts should be taken into account and again MnO_x can be good candidates for total oxidation of toluene. Lastly MnO_x are also recognized as efficient catalysts in CO oxidation which is also an important reaction to consider.

This review attempts to summarize our present state of knowledge using MnO_x-based catalysts for toluene abatement in PPC configuration. In that respect the presentation of the abundant manganese oxides will be firstly given. Then in a second step the main features of MnO_x allowing better performances in toluene total oxidation, ozone decomposition, toluene ozonation and CO oxidation will be successively briefly reviewed. Finally, in the last part the current status of the applications of PPC using MnO_x on toluene abatement will be discussed.

4.2. Presentation of the Main Manganese Oxide Structures

Manganese (Mn) is a multivalent element. Each valence state has a characteristic oxide or oxides. MnO_x occur naturally as minerals in at least 30 different crystal structures in a range of manganese oxidation states. Manganese oxides are technologically important materials and have widely been used as effective and inexpensive catalysts and as electrode materials for batteries. Interestingly, some MnO_x crystal structures exhibit tunnel and/or layered structures with varied proportions of Mn in different oxidation states (+2, +3, and +4). The known binary oxides of manganese include MnO, Mn_2O_3, Mn_3O_4 and MnO_2. Like many monoxides, MnO adopts the rock salt structure, where cations and anions are both octahedrally coordinated. The α-Mn_2O_3 phase is named bixbyite. The Mn^{3+} ions are octahedrally coordinated, while the O ions have 4 Mn neighbors. The bixbyite structure can be viewed as a close-packed lattice of Mn with O ions filling three quarters of the tetrahedral interstitials in a pattern with Ia3 symmetry. Hausmannite Mn_3O_4 has a spinel structure having a composition formula $Mn^{2+}(Mn^{3+})_2O_4$, where Mn^{2+} ions occupy the tetrahedral sites and Mn^{3+} the octahedral sites [23].

Along these oxides is the metastable layered Mn_5O_8 having a compositional formula $((Mn^{2+})_2(Mn^{4+})_3O_8)$. Manganese dioxide, MnO_2, for its own part, shows polymorphism. MnO_2 has several crystalline structures, including α-, β-, γ-, δ-, and λ-MnO_2. The different tunnel structures can be described by the size of their tunnels determined by the number of octahedral subunits ($n \times m$), as depicted in Figure 3. α-MnO_2 (hollandite) consists of double chains of edge-sharing MnO_6 octahedra, which are linked at corners to form 1D (2×2) and (1×1) tunnels in the tetragonal unit cell. The size of the (2×2) tunnel is 0.46 nm, which is a large tunnel for insertion/extraction of alkali cations. β-MnO_2 (pyrolusite) is composed of single strands of edges haring MnO_6 octahedra to form a 1D (1×1) tunnel. Because of the narrow (1×1) tunnel size (0.189 nm), β-MnO_2 cannot accommodate cations. The structure of γ-MnO_2 is random intergrowths of ramsdellite (1×2) and pyrolusite (1×1) domains. δ-MnO_2 is a 2D layered structure with an interlayer separation of 0.7 nm. It has a significant amount of water and stabilizing cations such as Na^+ or K^+ between the sheets of MnO_6 octahedra. λ-MnO_2 is a 3D spinel structure.

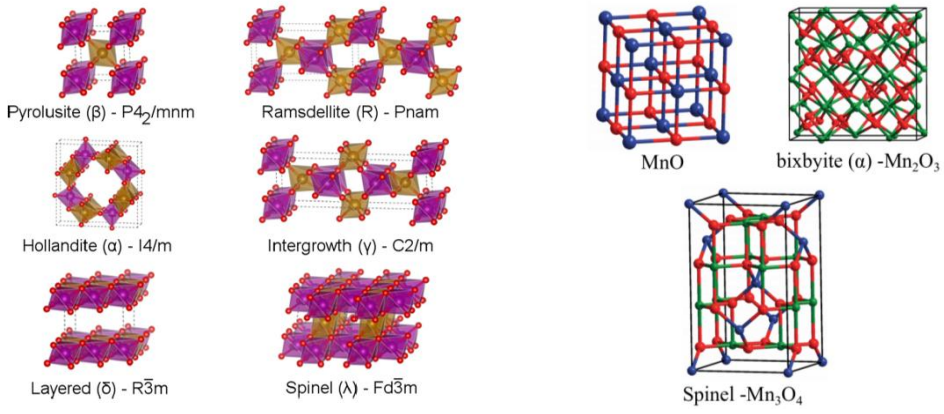

Figure 3. Illustration of the crystal structures of selected common manganese oxides: (**a**) MnO_2 including: α-$Mn^{IV}O_2$ (hollandite); rutile β-$Mn^{IV}O_2$ (pyrolusite); R-$Mn^{IV}O_2$ (ramsdellite); γ-$Mn^{IV}O_2$ (intergrowth); δ-$Mn^{IV}O_2$ (birnessite); λ-$Mn^{IV}O_2$ (spinel); Here, The purple and yellow atoms represent spin-up and spin-down Mn, respectively, while the red atoms represent O [24]; (**b**) Crystal structures of MnO, α-Mn_2O_3 and Mn_3O_4. The green, blue, and red atoms represent Mn^{III}, Mn^{II}, and O^{2-}, respectively [25].

The richness in MnO_x structures thus provides a rigorous test system to explore the significance of atomic positions on the catalytic efficiency towards toluene oxidation.

4.3. MnO_x in Catalytic Oxidation of Toluene

The high reactivity of MnO_x towards VOCs abatement is generally ascribed to easy variation of manganese oxidation state (Mn^{2+}, Mn^{3+}, Mn^{4+}), oxygen storage capacity in the crystalline lattice and high mobility of lattice oxygen [26]. Kim and Shim [27] investigated the effect of O/Mn stoichiometry using Mn_3O_4, Mn_2O_3 and MnO_2. It was found that the catalytic activity decreased in the order of Mn_3O_4 > Mn_2O_3 > MnO_2 in line with the decrease of the specific surface areas and oxygen mobility of the MnO_x. Mn_3O_4 [28], Mn_2O_3 [29,30] and MnO_2 [28] were also previously investigated separately by different research teams for toluene oxidation. F. Wang et al. [31] reported on the external morphology effect of MnO_x (rod-, wire-, tube-, and flower-like morphologies) for the oxidation of toluene. It was found that the oxygen ad-species concentration (related to the Mn^{3+} concentration) and low-temperature reducibility decreased in the order of rod-like α-MnO_2 > tube-like α-MnO_2 > flower-like Mn_2O_3 > wire-like α-MnO_2, in good agreement with the sequence of the catalytic performance of these samples. The best-performing rod-like α-MnO_2 catalyst could effectively catalyze the total oxidation of toluene at low temperatures (T_{50} = 210 °C and T_{90} = 225 °C at a GHSV of 20,000 $mL \cdot g^{-1} \cdot h^{-1}$). It was concluded that the excellent catalytic performance of α-MnO_2 nanorods might be associated with the high oxygen ad-species concentration and low-temperature reducibility. Verykios et al. [32] showed that γ-MnO_2 which was less affected by the presence of water than other MnO_2 polymorphs could be suitable for toluene removal. This catalyst was claimed to be more active than noble metal catalysts.

In a same way, various structures of MnO_2 i.e., α-, β-, δ-MnO_2 were prepared and their catalytic performances in toluene oxidation were assessed to those of a γ-like MnO_2 obtained by the selective removal of La^{3+} from an acid-treated three-dimensional macroporous and mesoporous $LaMnO_3$ [33]. The best performance of this γ-like MnO_2 over the other MnO_2 polymorphs was ascribed both to the open three-dimensional macroporous and mesoporous morphology leading to higher BET surface areas than conventional syntheses, enhanced surface adsorbed oxygen (O_{ads}) to lattice oxygen (O_{latt}) molar ratio (O_{ads}/O_{latt}) and easier reducibility. Similarly Liao et al. [34] investigated the external morphology effect over Mn_3O_4 having hollow and solid sphere morphologies for toluene abatement. The better catalytic activity when using hollow spheres of Mn_3O_4 was claimed to result from beneficial combined effects such as the cavity morphology leading to high surface area, higher O_{ads}/O_{latt} molar ratio, believed to be proportional to active oxygen, and higher Mn average oxidation state (AOS). MnO_x supported catalysts were affected by the same factors too. To conclude catalytic activity is generally associated with several factors, such as the BET surface area, presence of oxygen vacancies, reducibility, and external morphology of the catalyst.

The common oxidation catalytic reactions generally involved three types of mechanism [35]: Langmuir-Hinshelwood, Eley-Rideal and Mars-Van Krevelen (MkV) mechanism [33]. It is well known that MnO_x exhibit strong oxygen storage/release ability due to the fact that they easily undergo a rapid reduction–oxidation cycle through the interaction with reducing or oxidant agents accompany by the formation of manganese ions in various oxidation states. The involvement of lattice oxygen of catalysts in total oxidation of toluene and the strong correlation between labile lattice oxygen and catalytic activity suggest that the reaction could proceed via the MvK model [8,36]. In the case of VOCs catalytic oxidation, the first step corresponding to the reduction of the catalyst surface is generally the rate determining step [37].

4.4. MnO_x in Ozone Decomposition

Decomposition of ozone in the gas phase was carried out on various metal oxides by S. Imamura et al. [38]. It was shown that the activity of the metal oxide catalysts increased roughly in the order of the increase in their surface area and in the amount of surface oxygen on them. These observations are very interesting, as these characteristics resemble to those of total oxidation catalysts because low surface area and a small amount of surface oxygen are generally targeted for partial oxidation catalysts. Interestingly, metal oxide conductance increased throughout ozone

introduction for the most reactive oxides such as $Ag_2O \approx NiO$, CuO, Co_3O_4 which are p-type oxides suggesting that negatively charged oxygen species were formed on their surface. Ag_2O was claimed to be the most effective catalyst in decomposing ozone, increasing its activity as the reaction proceeds while some transition-metal oxides are deactivated during the reaction due to accumulation of oxygen species that cover their active sites. The high reactivity of the oxygen species on Ag was invoked to be due to the especially weak bond between oxygen and silver compared with those between oxygen and other metals. Additionally, the high reactivity of such catalyst for CO oxidation was believed to occur thanks to the production of very active oxygen such as oxygen ion O^- without totally discarding oxygen (O) and ozonide ion (O_3^-) resulting from the decomposition of O_2^-.

In that way, a comprehensive survey of different oxides (MnO_2, Co_3O_4, NiO, Ag_2O, Fe_2O_3, Cr_2O_3, CeO_2, MgO, V_2O_5, CuO and MoO_3) supported on γ-Al_2O_3 for ozone decomposition, but this time in the presence of water (RH (Relative humidity): 40%), was performed by B. Dhandapani et al. [39]. It is found again that p-type oxide semiconductors are the most active substances for ozone decomposition. Among the investigated transition metal oxides MnO_2 showed the highest activity explaining its prevalence in patent disclosures. The ozone decomposition pathway over MnO_x supported on γ-Al_2O_3 was investigated by T. Oyama et al. The reaction proceeds through two irreversible steps, the adsorption of ozone on the catalyst surface and the desorption of molecular oxygen [40,41]. Ozone is first decomposed/reduced by Mn^{n+} cation into O^{2-} and O_2. Then production of active O_2^{2-} and O_2 was proposed via reaction of O^{2-} with another O_3 molecule in the presence of $Mn^{(n+2)+}$. Next, unstable O_2^{2-} reduced $Mn^{(n+2)+}$ back into Mn^{n+} and desorption of an oxygen molecule occured [42,43]:

$$O_3 + Mn^{n+} \rightarrow O^{2-} + Mn^{(n+2)+} + O_2 \quad (1)$$

$$O_3 + O^{2-} + Mn^{(n+2)+} \rightarrow O_2^{2-} + Mn^{(n+2)+} + O_2 \quad (2)$$

$$O_2^{2-} + Mn^{(n+2)+} \rightarrow Mn^{n+} + O_2 \quad (3)$$

Oyama et al. found that the difference in the structure of the manganese active center was the origin of support effect on the activity. At low Mn loadings (<6 wt %) the active phase was to be well dispersed on Al_2O_3 but not well understood. Significant progresses were achieved in 2001 by R. Radhakrishnnan et al. by using extended X-ray absorption fine structure (EXAFS) to evaluate the local bonding environment in the MnO_x/γ-Al_2O_3 catalyst [43]. The catalyst (3 wt %) was prepared throughout incipient wetness impregnation using a manganese acetate precursor. After heating at 170 °C for 6 h, the solid was calcined at 400 °C. Based also on in situ Raman spectroscopy analysis performed before and during ozonation reaction and ab Initio calculations as complementary tools a four mononuclear species was postulated as the manganese active center with a Mn–O distance of 210 pm as shown in Figure 4. During the ozone decomposition reaction, an adsorbed peroxide species was observed on the catalyst surface (Raman line at 880 cm^{-1}).

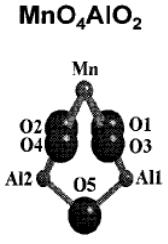

Figure 4. Geometry-optimized four oxygen coordinate Mn structure using the HF/6-311G method [43].

Only a few works have investigated the activity of manganese dioxides with specific crystal phase [44,45]. Ma et al. [46] proposed a scheme of ozone decomposition over transition metal doped cryptomelane–type manganese oxide catalysts (α-MnO_2) implying the $Mn^{3+/4+}$ mixed valence in the

decomposition/reduction of O_3 into O_2 and O^-. Consequently, the main differences here stem in the nature of the implied redox couple of manganese and in the nature of the reactive oxygen species: O^- instead of O_2^{2-}.

$$O_3 + (Mn^{3+}) \rightarrow O_2 + O^-_{ads}(Mn^{4+}) \quad (4)$$

$$O_3 + O^-_{ads}(Mn^{4+}) \rightarrow 2O_2 + (Mn^{3+}) \quad (5)$$

This scheme highlights the importance of the mixed valence ($Mn^{4+/3+}$) in α-MnO_2 catalysts. Based on this mechanism the higher content of Mn^{3+} (surface oxygen vacancies) cations present at the surface of the catalyst is expected to promote ozone decomposition.

Interestingly, the effect of MnO_2 structure on ozone decomposition was recently investigated on α-, β- and γ-MnO_2. The activity of these three MnO_2 polymorphs for ozone decomposition followed the order of α- > γ- > β-MnO_2. The superior performances of α-MnO_2 were explained by the combined largest specific surface area and the lowest Mn AOS. Additionally, it was found that the catalytic activity of MnO_2 strongly depended on the density of oxygen vacancies in line with the presence of Mn^{3+}. The ozone decomposition mechanism based on the involvement and recycling of oxygen vacancy (V_O) was proposed below and the pertinent points were grasped in Figure 5. Once Mn^{3+} appears in the manganese dioxide, oxygen vacancies were generated to maintain electrostatic balance according to the following process (Equation (6)):

$$4Mn^{4+} + O^{2-} \rightarrow 4Mn^{4+} + 2e^-/V_O + 1/2O_2 \rightarrow 2Mn^{4+} + 2Mn^{3+} + V_O + 1/2O_2 \quad (6)$$

$$O_3 + V_O \rightarrow O_2 + O^{2-} \quad (7)$$

$$O_3 + O^{2-} \rightarrow O_2 + O_2^{2-} \quad (8)$$

$$O_2^{2-} \rightarrow O_2 + V_O \quad (9)$$

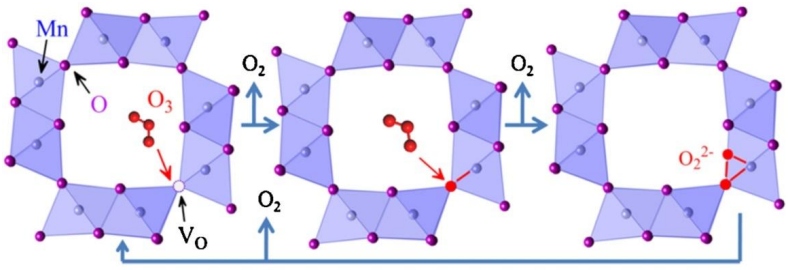

Figure 5. Ozone decomposition mechanism based on the involvement and recycling of oxygen vacancy (V_O) [44].

When ozone gas flows through MnO_2, the ozone molecule binds to MnO_2 surface by inserting an O atom into an oxygen vacancy site. The oxygen vacancy is 2-electron donor and transfers 2 electrons to an O atom of ozone [47,48], thus forming an oxygen species (O^{2-}) in the oxygen vacancy site and an oxygen molecule, which desorbs into the air (see Equation (7)). Then another ozone molecule reacts with O^{2-} to produce a gas-phase oxygen molecule and a bridging O_2 dimer (peroxide, O_2^{2-}), which was observed by in situ Raman spectroscopy (see Equation (8)). Finally, the peroxide species (O_2^{2-}) decomposes to release an oxygen molecule (see Equation (9)). The decomposition of peroxide species was believed to be the rate-limiting step.

This study brings important guidelines for the design of future MnO_2-based catalyst for ozone removal.

4.5. MnO_x in Ozonation Reactions

Catalytic ozonation is an innovative method for oxidation of pollutants in liquid or gas phase. Ozonation reactions mainly referred to catalytic VOCs oxidation by ozone. As this reaction consists of ozone decomposition in the presence of an organic substrate it is not surprising that MnO_x, which are among the most active transition metal oxides for low temperature decomposition of ozone to generate active oxygen species, are required for oxidation of VOCs by ozone. Application of this method in gas phase has opened a new catalytic approach for low temperature oxidation of VOCs at trace concentration levels. Results of the literature review show that apparent activation energy of VOCs oxidation can be greatly reduced by use of ozone compared to that of oxygen, making total oxidation of VOCs possible at temperatures as low as 100 °C or even lower.

Effect of manganese loading on total oxidation of toluene by ozone using MnO_x/γ-Al_2O_3 was investigated by E. Rezai et al. [49]. Activities of four loadings of Mn (1%, 5%, 10% and 20%) were studied in the temperature range of 22–100 °C. A direct relationship between Mn loading and average oxidation state of manganese was found. Catalysts at lower loadings, up to 10%, were mostly composed of Mn_2O_3 while a mixture of MnO_2 and Mn_2O_3 was present in catalysts with loadings higher than 10%. All catalysts became deactivated at room temperature and their activities were improved by an increase of temperature. It was observed that lower Mn loadings have higher activity in oxidation of toluene. It was proposed that lower oxidation states of manganese are more favorable in decomposition of ozone resulting in higher rate of toluene oxidation. A Langmuir–Hinshelwood mechanism based on activation of toluene molecule via abstraction of hydrogen from the methyl group was postulated to occur over MnOx/γ-Al_2O_3 (10 wt %) catalyst [50] explaining the effect of toluene and ozone partial pressures on toluene oxidation rate. Hence the C–H bond cleavage was assumed to be the relevant kinetic step in the oxidation of toluene by ozone.

The mechanism of oxidation of VOCs by ozone is based on ozone decomposition due to Equations (10)–(14) generating atomic oxygen to react with VOCs in the oxidation reaction (Equation (14)) assuming that VOCs are adsorbed on Mn sites (Equation (13)) and the reaction proceeds based on Langmuir-Hinshelwood mechanism between adsorbed species (Equation (14)) [49].

$$O_3 + Mn \rightarrow O_2 + O\text{-}Mn \quad (10)$$

$$O_3 + O\text{-}Mn \rightarrow O_2 + O_2\text{-}Mn \quad (11)$$

$$O_2\text{-}Mn \rightarrow O_2 + Mn \quad (12)$$

$$VOC + Mn \rightarrow VOC\text{-}Mn \quad (13)$$

$$VOC\text{-}Mn + O\text{-}Mn \rightarrow Products \quad (14)$$

It is believed that higher dispersion of Mn atoms in catalysts with lower loading levels decreases oxidation state of Mn.

XRD studies showed the presence of β-MnO_2 and Mn_2O_3 (bixbyite) in the Mn loading of 10%. The percentages of Mn_2O_3 and MnO_2 in the catalyst estimated from XANES spectra were 91.0% and 9.0%, respectively. The activation energy of the reaction was determined to be 31 kJ/mol obtained by a power law model. The power law model also determined the reaction orders with respect to toluene and ozone as −1 and 2, respectively [50].

Ozonation of toluene catalyzed by MnO_x supported on siliceous MCM-41 was also investigated by the same team [51]. The performances were found to be similar to those of MnO_2/γ-Al_2O_3 at room temperature, the activity decreasing with reaction time as the supported alumina catalyst.

MnO_2/graphene samples were developed for catalytic ozonation of toluene by M. Hu et al. [52]. The hydrothermal method was used as an effective way to prepare tightly anchored birnessite-type MnO_2 on graphene. The highest toluene degradation rate of 7.89×10^{-6} mol·min^{-1}·g^{-1} obtained over the 64.6 wt % MnO_2/graphene sample was attributed to a synergetic effect of graphene and MnO_2.

This synergetic effect was attributed to the tight connection between the active sites on graphene for adsorption of toluene and decomposition of ozone, and the MnO_2 on graphene for decomposition of ozone to form atomic oxygen species. Additionally, MnO_2/graphene can be regenerated at 325 °C.

MnOx dispersed on HZSM-5 (Mn/HZSM-5; Mn: 4 wt %) was shown to be an efficient catalyst for oxidation of 20 ppmv of toluene in the presence of 2000 ppmv of ozone at 30 °C [53]. It was shown by DRIFTS analysis a toluene and ozone conversions of about 78% and 70%, respectively, over Mn/HZSM-5 with a CO_x ($CO + CO_2$) selectivity of 70%. Additionally, the catalytic performances were promoted by Ag which was attributed to induce more oxygen vacancies. The high activity of these catalysts was mainly attributed to the reactive oxygen species generated from ozone decomposition over the oxygen vacancies of these catalysts. Based on the obtained results the possible reaction pathways with or without ozone were given in Figure 6. The toluene can be partially oxidized into benzyl alcohol by the lattice oxygen, but it can be further oxidized into benzaldehyde, benzoic acid and maleic anhydride, ultimately, mineralized to CO_2 by O_3 at room temperature.

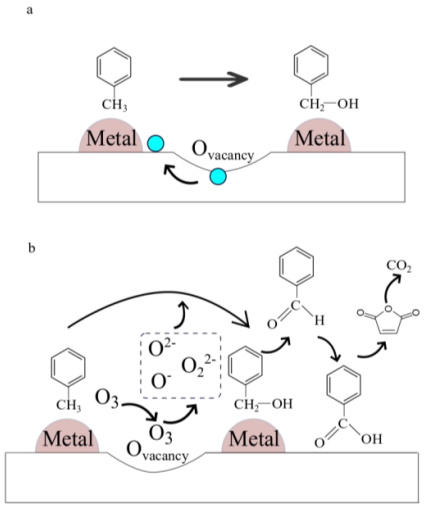

Figure 6. The pathway of toluene oxidation without ozone (**a**), with ozone (**b**) at room temperature adapted from [53].

Commercial honeycomb ozone decomposition catalyst (consisting of MnO_2 as the main active phase with SiO_2 and TiO_2) immobilized on a nonwoven fabric was investigated for O_3 and toluene removal in dry and humid conditions [54]. It was shown that O_3 was rapidly decomposed only around the entrance of the honeycomb ozone decomposition catalyst. However the amount of converted toluene decreased with time because water molecules competed on the catalyst surface decreasing O_3 and toluene adsorption. To overcome this inhibition MnO_2 catalysts were mixed with alumina or zeolite, which were functional adsorbents, to increase the contact between O_3 and the ozone decomposition catalyst (ODC) surface but however only a small percentage of VOCs reacted.

Table 3 exhibits the salient results in ozonation reactions towards toluene abatement. As mentioned above the active phase is mainly MnO_2 well dispersed on a support which is generally γ-Al_2O_3, TiO_2/SiO_2, graphene and HZSM-5. It has to be mentioned that graphene allows to dispersed huge amount of Mn (60 wt %) as compared to γ-Al_2O_3 where the Mn content does not exceed the value of 20 wt % [49,55]. All given reactions here are conducted at room temperature. Direct comparison of the different catalyst performances is complicated due to the discrepancy of the operating parameters such as the ratio of generated ozone to the inlet toluene ratio which ranged from 0.55 to 8.75. Beneficial effect is noticeable when this ratio is allowed to increase. Additionally, ozone consumption decreases whatever the catalyst under concern indicating partial deactivation of the catalyst. This decrease is always accompanied to a decrease of the toluene removal efficiency in line with poor carbon mass balance.

Table 3. Overview of ozonation results for toluene abatement.

Catalyst	Active Phase	Flow Rate (mL/min)	GHSV ($mL \cdot h^{-1} \cdot g^{-1}$)	Temperature (°C)	CC_7H_8 (ppm)	CO_3 (ppm)	O_3/C_7H_8	$\eta_{Toluene}$ (%)	η_{Ozone} (%)	By-Products	Reference
20% MnO_2/Al_2O_3	MnO_2	100 (dry air)	60,000	20	177	98	0.55	~25 (160 min) then deactivation	From 100 to 80% in 160 min	Benzoic acid, benzaldehyde, and benzyl alcohol.	[55]
10% MnO_x/γ-Al_2O_3	MnO_2 and Mn_2O_3	1000 (dry air)	300,000	20	120	1050	8.75	From 100 to 40% in 330 min	From 100 to 20% in 330 min	Acetic acid, oxalic acid, benzene and maleic anhydride Carbon balance: ~20%	[49]
65 wt % MnO_2/graphene	MnO_2	150 (dry air)	112,500	20	200	400	2	~33.6 (400 min) then deactivation	~84.3 (400 min), then deactivation	Organic byproducts	[52]
$MnO_2/TiO_2/SiO_2$ honeycomb	MnO_2	1000 (dry air)	-	20	10	38	3.8	~72 (100 min)	-	Carbon balance: ~22%	[54]
	MnO_2	1000 (RH: 70%)	-	20	10	38	3.8	~35 (100 min)	-	Carbon balance: ~50%	
Mn/HZSM-5	MnO_x	100 (dry air)	150,000	30	20	200	10	78	70	benzaldehyde, benzoic acid and maleic anhydride	[53]

Alcohols, aldehydes and organic acids were identified as intermediates in the reaction process. Heat treatment and excessive ozone feeding favored catalyst generation.

As catalytic ozonation proceeds at lower temperature compared with conventional catalytic oxidation processes, catalyst stability under mild conditions remains a problem. Although aromatic compounds can be oxidized by manganese oxide catalysts at room temperature in an ozone feed, the catalysts generally suffer from severe deactivation because of the build-up of less-reactive by-product compounds on the catalysts.

4.6. The Ability of MnO_x for CO Removal

Catalytic oxidation of CO has long been studied on various MnO_x catalysts due to their high CO oxidation ability and low cost in contrast to the expensive noble metal catalysts [56]. Like Cr, Mn has also been used in association with other elements, such as Cu, Co, Ni, and La, to form manganites, which are very active for CO oxidation [57].

In the study of CO oxidation by various bulk MnO_x at low temperature ($\leq$250 °C), Ramesh et al. [56] reported that the ranking for CO oxidation in a mixture of unit ratio of O_2/CO by decreasing activity followed the sequence: $Mn_2O_3 > MnO_2 \geq MnO$. The CO oxidation over MnO_2 and Mn_2O_3 occurred via Langmuir–Hinshelwood mechanism while over MnO a MvK mechanism prevailed. More energy was needed for activating the CO–Mn^{2+} bond in the reaction which accounted for the low activity of MnO. By opposition, the high reactivity for Mn_2O_3 was attributed not only to the moderate strength of CO–Mn^{3+} bond but also to the abundant defects/oxygen vacancies on its surface phase.

Interestingly, Wang et al. [58] compared the catalytic behavior of three manganese oxides (MnO_2, Mn_3O_4 and Mn_2O_3) doped or not by gold. Mn_2O_3 appeared to be the most active oxide (T_{50}: +135 °C), reducing at the lowest temperature and undergoing exceptional promotion by gold (T_{50}: −62 °C on 2.9% Au/Mn_2O_3). Imamura et al. [59] in their investigation of Pd/Mn_2O_3 catalysts found a similar high activity for the bare support. The role of Mn_2O_3 would be to permit the incorporation of O_2. The slow step would be the surface reaction of CO, which is promoted by Pd.

MnO_2 was also the subject of numerous investigations for CO oxidation [60–62]. As discussed above, MnO_2 has 4 kinds of polymorphs, denoted as α-, β-, δ-, γ-MnO_2. α- and δ-MnO_2 were found to be the most active phases for CO oxidation, whereas β- and γ-MnO_2 are much less active [60]. The order of activity was well-correlated to the Mn–O bond strength (α < δ < γ < β), the higher Mn–O bond strength, the lower the activity.

Liang et al. [60] also suggested that the oxidation state of manganese constantly oscillates between Mn^{4+} and Mn^{3+}. The γ- and β-MnO_2 polymorphs would be less active because the re-oxidation of Mn^{3+} into Mn^{4+} would be more difficult than in α- and δ-MnO_2. This was also confirmed by the work of Iablokov et al. [63].

Among the most common Mn-based oxides, Mn_2O_3 was the most reactive in CO oxidation, and among the different polymorphs of MnO_2, α- and δ-MnO_2 were found to be the most active phases. It should be noted, however, that Iablokov et al. [63] were able to prepare an efficient MnO_x ($1.61 < x < 1.67$) oxide, more active in CO oxidation than Mn_2O_3, via calcination of a manganese oxalato precursor in 10% O_2 at 525 °C.

5. MnO_x in PPC for Toluene Abatement

PPC is a two-stage plasma-catalysis system, including two reactors in series with the catalytic reactor located downstream of NTP. The operating mode is the following: the gaseous effluent, consisting of the VOC generally diluted in moist air, is processed by the NTP. The chemical effects occurring within the plasma are the result of an energy injection into the gas effluent by way of electron-impact processes under an electric field. Complex homogeneous reactions take place between the plasma generated reactive species enabling the more or less complete decomposition of the initial VOC. The nature and extent of these homogeneous reactions depend mainly on the energy put per liter in the plasma and to the type of discharge all other things otherwise remaining equal. Usually the NTP

can degrade the VOC to some extent but the main drawbacks are high energy consumption and its non-selectivity. Consequently organic intermediates which can be more harmful than the starting VOC, along with hazardous substances such as O_3 and NO_2, can evolve from the NTP reactor. By opposition to IPC where the catalyst is integrated in the reactor, the plasma produced short-lived reactive species do not achieve to reach the catalytic reactor in PPC configuration.

Hence the NTP process can lead to the formation of a complex gaseous product distribution. At that stage the design of the catalyst plays a key role to improve CO_2 selectivity. Indeed the catalyst should be able to transform all the hazardous species into CO_2 taking advantage of active oxygen species from ozone decomposition. Hence once more the catalyst should exhibit high performances in ozone decomposition. Comparing to ozonation reactions where the plasma plays only the role of ozone supplier (ozoner), in PPC, plasma processes alter the gas composition that is fed to the catalyst in a complex manner. In a previous study A. Gervasini et al. investigated the role of the plasma as ozoner and in PPC configuration for the abatement of various VOCs [64]. It resulted that plasma driven catalysis was more efficient than gaseous ozonation for waste gas treatment due to an "ionizing effect". It was put forwards that plasma could decompose or shatter the organics arranging molecules to be more easily destroyed by the catalyst. Anyway some additional works have to be carried out to ascertain such assumptions.

5.1. Current Applications of MnO_x Catalysts in PPC Systems for Toluene Abatement

5.1.1. The Characteristics of MnO_x in PPC

This part reviewed the performances of post-plasma catalysis towards toluene abatement focusing in particular on the characteristics of MnO_x used as catalyst downstream the plasma reactor. Two Tables have been included in this part for ease of reading. Table 4 compiles information on the synthesis and physico-chemical properties of the catalysts while Table 5 includes the salient parameters generally considered to play a role in the performances for toluene removal in PPC. From a close look at Table 4 it is found that the catalytic formulations, when considering homemade catalysts, include bulk MnO_x as single transition metal (TM) oxide [65,66] or as manganese phosphate Mn–O–P [67] or more usually in a combination with another TM (Cu [65,68–71], Co [66,72], Fe [68,73,74]) with the possible use of Ag as additive [75]. The active phase can be dispersed on a support such as γ-Al_2O_3, AC (activated carbon) [74], Ni foam [76] and ZSM-5 [72].

Bulk MnO_x were prepared by the conventional precipitation method at pH 9–10 using Mn(II) nitrate as precursor. L. Ye et al. [66] obtained a mixture of Mn_2O_3 and of the metastable Mn_5O_8 with a specific surface area close to 28 m^2/g after calcination at 400 °C. Quoc An et al. [65] reported the preparation of bulk α-MnO_2 (OMS-2) by the redox method performed at 100 °C for 24 h at pH 1.2 using $KMnO_4$ and $MnSO_4$ as Mn precursors in hydrothermal conditions. Magureanu et al. reported the synthesis of manganese phosphate [67]. Three amorphous Mn–O–P catalysts with Mn/P ratios of 1:1.5 (Mn-1), 1:0.04 (Mn-2) and 1:1 (Mn-3) were prepared from the reaction of MnO_2 with concentrated H_3PO_4 in aqueous/aminoalcohol medium via hydrothermal treatment (Mn-1) but under microwave conditions (Mn-2; Mn-3) using structure directing agents. The final catalysts were obtained after calcination at 550 °C. The increase of Mn loading led to an increase in specific surface area (4.5, 20 and 85 m^2/g for Mn-1, Mn-2 and Mn-3, respectively) accompanied with a change in the pore size distribution from microporous to mesoporous. The XPS Mn AOS showed values less than 4 due to Mn reduction in the presence of the template.

As MnO_x exhibit many structures the characterization of the catalyst can be very tricky when dispersed on a support. The parameters which are the most relevant to affect the structure and dispersion are the nature of the Mn precursor, the mode of impregnation, the temperature of calcination, the nature of the support and the Mn content. As shown in Table 4, the MnO_x/γ-Al_2O_3 have all been prepared via wetness impregnation of Al_2O_3 with manganese nitrate and calcined at temperature in the range 350–400 °C with Mn amount ranging from 7 to 10 wt % [66,74,77]. It has been found that the

nitrate precursor leads to mainly β-MnO_2 for a Mn loading of 10 wt % over γ-Al_2O_3 at a calcination temperature of 400 °C for 4 h [78]. However decreasing the temperature of calcination is expected to increase the dispersion and change the Mn AOS.

Manganese (Mn: 3 wt %) was also dispersed by wet impregnation using manganese (II) acetate as Mn precursor on an activated carbon (AC) developing very high surface area (1308 m^2/g) [74]. The MnO/AC catalyst was obtained after calcination at 300 °C in N_2 for 2 h. The low Mn content, the counter-anion nature of the Mn precursor as well as the conditions of calcination ensured a good Mn dispersion combined to a low Mn AOS. Mn_2O_3 deposited on nickel foam was reported by H. Huang et al. [76]. The Ni foam was a special support having a thin and porous structure enabling the pressure drop in the reactor to be greatly reduced. The formation of Mn_2O_3 resulted here from a calcination of the Mn nitrate dispersed on Ni foam at a temperature of 600 °C.

Although Ag-Mn/HZSM5 showed good activity in the ozonation of toluene, low cost Ag-free multi-component catalysts were investigated to increase the performances. As previously noticed, a second transition metal (TM such as Cu, Fe and Co) can be integrated in combination with Mn. Among the three TM oxides, Fe_2O_3 and Co_3O_4 are p-type metal oxides recognized for having high activity in ozone decomposition by opposition to CuO which is a n-type oxide [39]. However mixing Cu with Mn could lead to hopcalite catalysts recognized as efficient catalysts in O_3 removal [79] and CO oxidation at room temperature [80]. The occurrence of the two redox couples Cu^{2+}/Cu^{+} and Mn^{4+}/Mn^{3+} in the solid was believed to play a role in these catalytic reaction [81]. Additionally, the Cu–Mn–O system was remarkably active in toluene oxidation [8,82–89]. Beside, enhanced ozone decomposition over Fe–Mn oxides was explained by a lower MnO_2 crystallite mean size, a more defective structure and improved textural properties [90].

Quoc An et al. [65] reported the dispersion of copper (5 wt %, 10 wt % and 15 wt %) on α-MnO_2 using wetness impregnation method with nitrate Cu precursor followed by a calcination at 500 °C for 4 h. However no physico-chemical characterizations can help to the comprehension of the structure of these catalysts. Ye et al. reported the synthesis of Co–Mn oxides (Co/Mn atomic ratio of 1:6, 1:1 and 6:1) using the co-precipitation at pH 9–10 using Mn and Co nitrate precursors [66]. The calcination step was performed at 400 °C for 2 h. XRD analysis revealed Mn_3O_4, $Co_3Mn_3O_4/Co_3O_4$ and Co_3O_4 for the three increasing Co/Mn ratios, respectively. Hence the Co/Mn ratio of 1.0 allowed a good mixing of Mn and Co in the presence of segregated oxides. Textural properties were improved for the stoichiometric and Co rich catalyst allowing to double the specific surface area in comparison with the MnO_x reference catalyst. Additionally, the XPS Mn AOS increased when incorporating Co in line with larger number empty d-states and greater reducibility (electron accepting nature) of the active center.

Recently, Y. Huang reported the synthesis of 10 wt % of $CoMnO_x$ and $CeMnO_x$ (M/Mn = 1; M = Co, Ce) active phases supported on ZSM-5 and of a reference MnO_x/ZSM-5 catalyst [72]. The textural properties of the porous support ZSM-5 were the following: BET surface area of 306 m^2/g and average pore size of 9.1 nm. These catalysts resulted from a coprecipitation at pH 9–10 using nitrate precursors followed by a calcination step at 400 °C for 5 h. The reference MnO_x/ZSM-5 revealed a complex mixture of Mn_3O_4, Mn_2O_3 and MnO_2. The Co-based catalyst exhibited the mixed $Co_3Mn_3O_4$ phase in accordance with Ye et al. [66]. By opposition only single oxides such as Ce_2O_3, MnO_2, and Mn_3O_4 were observed on the Ce-containing catalyst.

Table 4. The characteristics of Mn oxides in PPC.

Exp.	Catalyst	The Shape of Catalyst	The State of Catalyst	The Support	The Nature of Catalyst	Structure(s) (XRD)	The Synthesis Method/ Commercial Company	S_{BET} (m^2/g)	Dp [1] (nm)	Added Characterizations	Reference
1	$Cu–Mn/Al_2O_3$	Powder	Supported	Al_2O_3	Cu-Mn	-	Heraeus, Hanau, Germany	-	-	-	[70]
2	(a) N 150 (MnO_2–Fe_2O_3)	Pellet	Bulk	-	60 wt % Fe_2O_3 & 40 wt % MnO_2	MnO_2	Süd-Chemie (Munchen, Germany)	219	-	-	[74]
	(b) MnO_2/γ-Al_2O_3	Powder	Supported	γ-Al_2O_3	9 wt % MnO_2		Incipient wetness impregnation, Precursor: Mn nitrate, calcined at 350 °C for 2 h under 100 mL/min air	169			
	(c) MnO/AC			AC [2]	3 wt % MnO_2		Wet impregnation, Precursor: Mn acetate, calcined at 300 °C for 2 h under N_2	1024			
3	(a) Mn-1 (Mn–P–O)	Powder	Bulk	-	Mn–P–O	Amorphous phase	Hydrothermal: MnO_2 with H_3PO_4 (85 wt %) (Mn:P 1:1.5) in 50 mL distilled water + dimethylaminoalcohol, 170 °C for 48 h	4.5	-	XPS: Mn $2p_{3/2}$: oxidation state of Mn < 4; P $2p_{3/2}$: inorganic phosphates	[67]
	(b) Mn-2 (Mn–P–O)				Mn–P–O		Hydrothermal treatment under microwaves: starting gel: 1.00 P: 0.04 Mn: 0.48 HDTMABr [3]: 0.48 TMAOH [4]: 174.00 H_2O, 60 °C (1 h), 80 °C (1 h), and 300 °C (3 h) then calcination at 550 °C	21	1.1		
	(c) Mn-3 (M–P–O)				Mn–P–O		Starting gel: 1.00 P: 1.00 Mn: 0.48 HDTMABr : 0.48 TMAOH: 174.00 H_2O, same operating mode than above	85	3.4, 50		
4	$CuMn/TiO_2$	Pellets	Supported	TiO_2	3% Cu, 6.8% MnO_2	-	Heraeus, Hanau, Germany	50	-	-	[71]
5	MnO_2/Al_2O_3	Pellets	Supported	Al_2O_3 [5]	7 wt % MnO_2	-	Wetness impregnation Precursor: Mn nitrate, calcined at 400 °C	-	-	-	[77]
6	Mn_2O_3/Ni foam	Foam	Supported	Ni foam	Mn_2O_3	Mn_2O_3	Impregnation Precursor: Mn nitrate, calcined at 600 °C	10.8	-	XRD: before 400 °C, ultra-fine or amorphous features of phase. After 500 °C, Mn_2O_3	[76]
7	(a) $Cu–Mn/TiO_2$ (a)	Pellet (1.5 mm)	Supported	TiO_2	CuO (3 wt %) MnO_2 (6.8 wt %)	-	Hereaus Hanau, Germany	32	-	-	[68]
	(b) $Cu–Mn/TiO_2$ (b)					-		50	-	-	
	(c) Fe_2O_3-MnO_2 (N 150)	Pellet (6 mm)	Bulk	-	>40 wt % Fe_2O_3 >25 wt % MnO_2	-	Süd-Chemie (Munchen, Germany)	100	-	-	
	(d) CuO-MnO_2 (N 140)	Pellet (5 mm)			>15 wt % CuO >25 wt % MnO_2	-		100	-	-	

Table 4. *Cont.*

Exp.	Catalyst	The Shape of Catalyst	The State of Catalyst	The Support	The Nature of Catalyst	Structure(s) (XRD)	The Synthesis Method/ Commercial Company	S_{BET} (m^2/g)	Dp [1] (nm)	Added Characterizations	Reference
8	Fe_2O_3-MnO_2	Honeycomb [6]	Bulk	-	60 wt % Fe_2O_3, 30 wt % MnO_2	-	Süd-Chemie (Japan)	-	-	-	[73]
9	(a) MnO_2/Aluminum honeycomb	Honeycomb	Supported	Aluminum honeycomb	MnO_2	-	Honeycle ZA (Nichias Corporation)	-	-	-	[69]
	(b) MnO_2-CuO	Pellet (4–6 mesh)	Bulk	-	MnO_2-CuO	-	Moleculite (Molecular Products Limited)	20–30	-	-	
10	(a) OMS-2	Powder	Bulk	-	α-MnO_2	-	Hydrothermal treatment, Redox method, Precursors: $KMnO_4$ + $MnSO_4$ 100 °C for 24 h, pH: 1.2, calcined in static air using a range of time and temperature	-	-	-	[65,91]
	(b) Cu-OMS-2		Supported	OMS-2 [7]	5 wt % Cu	-	Wetness impregnation, Precursor: $Cu(NO_3)_2$ Calcined at 500 °C for 4 h	-	-	-	
	(c) Cu-OMS-2				10 wt % Cu	-		-	-	-	
	(d) Cu-OMS-2				15 wt % Cu	-		-	-	-	
11	Ag–Mn–O	Powder	Bulk	-	10 wt % Ag-MnO_x	Mn_3O_4 + Ag	Ag–Mn–O: Co-precipitation, pH 10, Precursors: $Mn(NO_3)_2$ + $AgNO_3$ dried at 110 °C for 12 h	-	-	-	[75]
12	(a) MnO_x	Powder	Bulk		MnO_x	Mn_3O_4 + Mn_5O_8	Precipitation, pH 9–10 Precursor: Mn nitrate, then calcined at 400 °C for 2 in air.	27.9	-	XPS: lattice oxygen 53.1%	[66]
	(b) Co_3O_4-MnO_2				1:6 = Co:Mn	Mn_3O_4	Coprecipitation at pH 9–10, Precursor: Mn and Co nitrates calcined at 400 °C for 2 h under in air.	29.5		XPS: lattice oxygen 56.2%	
	(c) Co_3O_4-MnO_2				1:1 = Co:Mn	$Co_3Mn_3O_4$ + Co_3O_4		53.4		-	
	(d) Co_3O_4-MnO_2				6:1 = Co:Mn	Co_3O_4		61.6		-	
13	(a) MnO_x/ZSM-5	Powder	Supported	ZSM-5	10 wt % MnO_x	MnO_2,Mn_2O_3, and Mn_3O_4	Precipitation, pH 9–10, calcined at 400 °C for 2 h in under air. Then wet impregnation with ZSM-5, calcined at 400 °C for 5 h	290.7	3.4	XPS: lattice O at 532.9 eV: 55.2%	[72]
	(b) $CoMnO_x$/ZSM-5				10 wt % $CoMnO_x$ (Co/Mn = 1)	$Co_3Mn_3O_4$, MnO_2 and Mn_3O_4	Coprecipitation. Same experimental procedure than above	302.8	2.9	XPS: lattice O at 532.9 eV: 59.2%	
	(c) $CeMnO_x$/ZSM-5				10 wt % $CeMnO_x$ (Ce/Mn = 1)	CeO_2, Ce_2O_3, MnO_2, and Mn_3O_4		305.6	2.9	XPS: lattice O at 532.9 eV: 58.3%	

[1] Pore diameter; [2] Activated carbon; [3] Hexadecyltrimethylammonium bromide; [4] Tetramethylammonium hydroxide; [5] Al_2O_3: diameter of granules being 3–4 mm and total surface area being 180 m^2/g; [6] Diameter: 15 mm, length: 75 mm, 500 cells per inch; [7] OMS-2: cryptomelane type manganese octahedral molecular sieve.

Table 5. Overview on toluene removal with MnO_x-based catalysts in PPC.

Exp.	Discharge Type (NTP Reactor)	Catalyst (weight/g)	Configuration	Carrier Gas Flow Rate (mL/min)	Toluene (ppm)	RH (%)	Inlet Ozone (ppm)	Inlet Ozone/Inlet Toluene	GHSV ($mL \cdot g^{-1} \cdot h^{-1}$)	MRE [1] (%)	ED [2] (J/L)	EY [3] (g/kWh)	$S_{CO2}/(S_{CO})$ (%)	Y_{CO2} (%)	By-Products CB [4]	Reference
1	Positive Corona discharge (pin-plate)	Cu–Mn/Al_2O_3 (-)	PPC	Air 133,600	45	-	60	1.3	-	22.8	18.7	8	-	-	-	[70]
		-	NTP	Air 133,600	45	-	-	-	-	10.8	18.7	4	-	-	-	
2	Glass beads packed bed DBD (cylindrical reactor)	(a) N 150 (MnO_2–Fe_2O_3) (1)	PPC	Air 315	240	-	-	-	18,900	76	172	14.4	23.5 (16.5)	17.9	CB [2]: 52.6%; O_3: 3.9 ppm	[74]
		(b) MnO_2/γ-Al_2O_3 (1)				-	-	-		88		16.7	18 (14)	15.8	CB: 36.3% O_3: 14.6 ppm	
		(c) MnO/AC (1)				-	-	-		99.7		18.9	30.2 (24.8)	30.1	CB: 55%. O_3: 8 ppm	
		-	NTP	Air 315	240	-	-	-	18,900	36	172	6.9	6	2.2	S_{CO}: 8%, CB: 38.8% O_3: 8 ppm	
3	DBD (Cylindrical reactor)	(a) Mn-1 (Mn–P–O) (0.2)	PPC	Air 300	200	-	6000	30	90,000	90–95	1400	1.7–1.8	73 (27)	65.7–69.4	CB: ~100%	[67]
		(b) Mn-2 (Mn–P–O) (0.2)				-		30					72 (28)	64.8–68.4	CB: ~100%	
		(c) Mn-3 (Mn–P–O) (0.2)				-		30					68 (32)	61.2–64.6	CB: ~100%	
		-	NTP	Air 300	200	-	-	-	90,000	70–75	1400	1.3–1.4	-	-	-	
4	Positive DC corona discharge (Pin-plate)	$CuOMnO_2$/TiO_2 (10)	PPC	Air 10,000	0.5	-	~18	36	60,000	78	2.5	2.1	-	-	NO_2: ~550 ppm at 15 J/L	[71]
		-	NTP	Air 10,000	0.5	27	-	-	60,000	4	2.5	0.1	-	-	-	
5	$BaTiO_3$ packed bed DBD (Cylindrical reactor)	7 wt % MnO_2/Al_2O_3 (7 mL)	PPC	Air 1000	500	-	-	-	60,000	97 [5]	60	-	-	-	CO: ~300 ppm	[77]
		-	NTP	Air 1000	500	-	-	-	8600 h^{-1}	74 [5]	60	-	-	-	-	
6	DBD (wire-plate)	Mn_2O_3/Ni foam (-)	PPC	Air 200	100	-	150	1.5	-	82	700	1.6	-	-	Ozone: 9 ppm	[76]
		-	NTP			-	-	-	-	44	700	0.8	-	-	-	
7	Positive DC corona discharge (pin-plate)	(a) Cu–Mn/TiO_2(a) (15)	PPC	Air 10,000	0.5	50	~70	140	40,000	40	14	0.19	-	-	-	[68]
		(b) Cu–Mn/TiO_2(b) (15)					~100	200		63	20	0.21	-	-	-	
		(c) Fe_2O_3-MnO_2 (N 150) (15)					~82	164		34	15.8	0.14	-	-	-	
		(d) CuO-MnO_2 (N 140) (15)					-	-		47	-	0.20	-	-	-	

Table 5. *Cont.*

Exp.	Discharge Type (NTP Reactor)	Catalyst (weight/g)	Configuration	Carrier Gas Flow Rate (mL/min)	Toluene (ppm)	RH (%)	Inlet Ozone (ppm)	Inlet Ozone/Inlet Toluene	GHSV ($mL \cdot g^{-1} \cdot h^{-1}$)	MRE [1] (%)	ED [2] (J/L)	EY [3] (g/kWh)	$S_{CO2}/(S_{CO})$ (%)	Y_{CO2} (%)	By-Products CB [4]	Reference
8	DBD (tubular reactor)	Fe_2O_3-MnO (-)	PPC	Air 2500	85	-	330	3.9	-	67	72	10.7	-	13 [4]	Gas: Benzene Solid: benzaldehyde, methylbenzoquinone, benzyl alcohol, benzoic acid, and benzyl benzoate	[73]
		-	NTP	Air 2500	85	-	-	-	-	18	72	2.8	-	7 [4]	Formic acid, Acetic acid and benzene	
9	Multistage reactor	(a) MnO_2/ Aluminum honeycomb (-)	PPC	Air +10,000	70	-	766	10.9	-	100	342	2.8	16.3	16.3	CO: 48 ppm; N_2O:18 ppm	[69]
		(b) MnO_2-CuO (-)						10.9	-	100			14.7	14.7	CO: 8 ppm; O_3: 117 ppm; N_2O: 21 ppm	
		(c) MnO_2/ Aluminum honeycomb+ MnO_2-CuO (-)						10.9	-	100			22.4	22.4	CO: 10 ppm; N_2O: 18 ppm	
		-	NTP	Air 10,000	70	-	-	-	-	~36	342	1.0	10.8	3.9	CO: 16 ppm; O_3: 1327 ppm; N_2O: 23 ppm	
10	DBD (Cylindrical reactor)	(a) OMS-2 (0.2)	PPC	80% N_2 +20% O_2 + 66.67		-	-	-	20,000	65	18 kV and 50 Hz	-	-	-	-	[65,91]
		(b) 5 wt % Cu-OMS-2 (0.2)				-	-	-		67		-	-	-	-	
		(c) 10 wt % Cu-OMS-2 (0.2)				-	-	-		68		-	-	-	-	
		(d) 15 wt % Cu-OMS-2 (0.2)				-	-	-		66		-	-	-	-	
		-	NTP	80% N_2 + 20% O_2 + 66.67	800	-	-	-	20,000	60		-	-	-	-	
11	DBD (tubular reactor)	Ag–Mn–O (0.2)	PPC	Air + 498	108	-	650	6.0	150,000	100	60	24.3	-	-	N_2O and CO	[75]
		-	NTP	Air + 498	108	-	-	-	150,000	60	60.	14.6	-	-	O_3:650 ppm N_2O and CO	

Table 5. *Cont.*

Exp.	Discharge Type (NTP Reactor)	Catalyst (weight/g)	Configuration	Carrier Gas Flow Rate (mL/min)	Toluene (ppm)	RH (%)	Inlet Ozone (ppm)	Inlet Ozone/Inlet Toluene	GHSV ($mL \cdot g^{-1} \cdot h^{-1}$)	MRE [1] (%)	ED [2] (J/L)	EY [3] (g/kWh)	$S_{CO2}/(S_{CO})$ (%)	Y_{CO2} (%)	By-Products CB [4]	Reference
12	DBD (tubular reactor,)	(a) MnO_x	PPC	Air + 500	107	-	580	5.4	32,233 h^{-1}	71	48	21.5	-	-	O_3: 280 ppm N_2O, CO	[66]
		(b) (1:6) Co_3O_4-MnO_2						5.4		84		25.5	-	-	O_3: 180 ppm N_2O, CO	
		(c) (1:1) Co_3O_4-MnO_2						5.4		93		28.1	-	-	O_3: 90 ppm N_2O, CO	
		(d) (6:1) Co_3O_4-MnO_2						5.4		83		25.0	-	-	O_3: 110 ppm N_2O, CO	
		-	NTP	Air + 500	107	-	-		32,233 h^{-1}	~24	48	7.3	-	-	-	
13	DBD (tubular reactor)	(a) MnO_x/ZSM-5	PPC	Air + 1000	107	12 mL/min air bubbling water	-	-	-	68	320	3.1	50 (8)	34	N_2O, O_3: 370 ppm	[72]
		(b) $CoMnO_x$/ZSM-5					-	-		94		4.3	78 (8)	73.3	N_2O, O_3: 200 ppm	
		(c) $CeMnO_x$/ZSM-5					-	-		86		3.9	70 (8)	60.2	N_2O, O_3: 260 ppm	
		-	NTP	Air + 1000	107		-	-	-	~37	320	1.7	-	-	-	

[1] MRE: Maximum removal efficiency; [2] ED: Energy density; [3] EY: Energy yield; [4] Carbon balance; [5] PPC and NTP experiments performed at 330 °C; [6] Y_{COx} (CO + CO_2).

5.1.2. The Performances in Toluene Abatement Using MnO_x in PPC

In a first step, the selected variables of the hybrid process related to the experimental conditions of toluene abatement in air were identified. The selected variables were those expected to play a role in the performances of the two-stage plasma-catalyst system towards toluene abatement. The descriptors linked to the performances of the hybrid process in terms of efficiency of the process were also presented. In a second step the effect of these variables on the experimental outcomes (descriptors) was discussed.

Based on data given in the literature the pertinent variables which can play a role have been identified and are related to the NTP reactor (geometry and type of discharge), the (specific) energy density at maximum of toluene conversion, nature of the gaseous effluent, type, shape and weight of the catalyst, GHSV, carbon balance and identified gaseous by-products. Information on the nature of the gaseous effluent includes variables such as kind of the carrier gas, flow rate, inlet toluene concentration and inlet ozone concentration injected into the catalytic reactor. When possible the same type of information is delivered in similar NTP experiments for easier comparison. Information on PPC performances towards toluene abatement includes the following descriptors: toluene removal efficiency associated with the energy put per plasma liter, CO_2/CO selectivity (S_{CO2}/S_{CO}), CO_2 yields (Y_{CO2}) and energy yield (EY).

Table 5 compiles the salient information on the application of post-plasma catalysis using MnOx-based type catalysts for toluene abatement in air in accordance with the above paragraphs.

First of all, the types of discharges were briefly discussed based on the information given in Table 6. Two discharge types were commonly used, such as DBDs (dielectric barrier discharges) with tubular/cylindrical configuration of the NTP reactor [65–67,72–75] or packed bed DBDs (packing material: glass [69] or $BaTiO_3$ [77]) and positive DC (direct current) corona discharge with pin-to-plate configuration [68,70,71].

The most important characteristic of DBDs is that non-equilibrium plasma conditions can be provided in a much simple way. At about atmospheric pressure electrical breakdown occurs in many independent thin current filaments due to the presence of the dielectric. The reactors are generally of tubular/cylindrical forms. These short-lived micro-discharges have properties of transient high pressure glow discharges with electron energies ideally suited for exciting or dissociating background gas atoms and molecules. The flexibility of the NTP reactor with respect to geometrical configuration, operating medium and operating parameters is well recognized. Efficient available low cost power supplies and additionally easy scaling up for laboratory experiments to large industrials installations taking into account the drawback of high pressure drop make DBDs attractive [92].

The presence of a packing material in the reactor leads to a packed bed DBD reactor. The promising utilization of such reactor is that the dynamics of plasma discharges are predominantly influenced by the properties of the packing material in terms of its dielectric constant. Increasing the dielectric constant enhances the electric field in the vicinity of pellets contact points [93]. Consequently the dielectric constant of a packing material determines the amount of energy that the reactor can store during a single discharge [94].

A corona discharge is an electrical discharge brought on by the ionization of a fluid such as air surrounding a conductor that is electrically charged. Corona discharges take place at or near atmospheric pressure using relatively low power. Corona discharge is a self-sustained discharge which occurs in sharply non-uniform electric field, typically operated in needle-to-plate or wire-to-plate configuration. Corona discharge mainly produces burst pulses corona, then streamer corona, glow corona and spark discharge as the applied voltage increases. Once the streamer corona discharge is formed in a closed chamber, a low temperature dense plasma environment can be generated over a large volume [92]. Hence, corona discharge is another approach that can avoid spark formation in streamer channels. The streamers propagation affects the NTP reactions like ionization, excitation, dissociation for VOCs abatement [20].

The experiments listed in Table 5 are all carried out at room temperature and atmospheric pressure except Exp.5 for which the catalyst has been heated at 330 °C. Dry air is used as carrier gas if nothing is mentioned otherwise. The total flow rate and the toluene concentration range from 67 to 133,600 mL·min^{-1} and 0.5 ppmv (indoor pollution) to 800 ppmv (range of industrial emission), respectively. The GHSV ranges from about 19,000 to 150,000 mL·g^{-1}·h^{-1}. These extreme values show the wide range of plasma-catalysis application in terms of volume and VOC concentration for treating a waste gas containing toluene. However it has to be mentioned that initial toluene concentration is close to 100 ppmv in most reported studies. The concentrations of ozone at the inlet of the catalytic reactor vary tremendously from 70 to 6000 ppmv depending on the nature of the NTP and to the inlet concentration of toluene. To get read of the influence of the initial toluene concentration the inlet ozone/inlet toluene molar ratio has been given. The values exhibited in Table 5 range herein from 1.3 to 200.

To evaluate the efficiency of the NTP reactors in terms of geometry-discharge, the toluene conversion has been plotted as a function of ED as shown in Figure 7. With that respect the characteristics of the NTP reactors have been recalled in terms of geometry and discharge and initial inlet toluene concentration $[C_7H_8]_0$ as shown in Table 6. The gap between the 2 electrodes ranges from 2 to 10 mm. The reactor volume V_R ranges from 8.5 to 250 mL and the corresponding residence time (t_r) ranges from 1.4 to 2.5 s except in Exp.1 for which the residence time is very short (4.5×10^{-4} s). The toluene removal efficiencies using corona discharge (Exp.1 and Exp.4) are relatively low compared to those of DBD (Exp.5 and Exp.11) for similar energy density. However this observation has to be tempered as the inlet toluene concentrations associated to corona discharge are rather low (45–0.5 ppmv) compared to those for DBD (100–500 ppmv). However among DBD reactors it is found that Exp.3 and Exp.5 lead to similar toluene conversion but with an energy density ratio ED(Exp.5)/ED(Exp.3) of about 24 noticeably higher than the inlet toluene concentration ratio of 2.5. The $BaTiO_3$ packed bed DBD reactor (Exp.5) exhibited herein the highest toluene removal efficiency (74%) at the lowest ED (60 J/L) thanks to the presence of $BaTiO_3$ which enhances the average electric field and to the temperature of the catalytic reactor at 330 °C. In this set of experiments, the effect of the residence time t_r in the NTP reactor is difficult to apprehend as the range of values is too narrow to allow a pertinent discrimination.

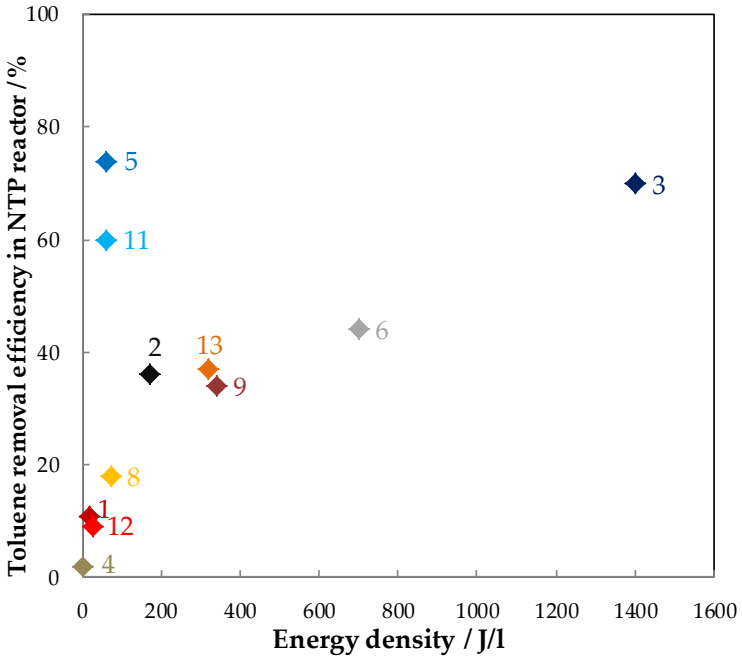

Figure 7. Toluene removal efficiency as a function of ED for NTP reactor. The figures mentioned inside the graph refer to the number of the experiment (see Tables 4 and 5).

Table 6. Characteristics of the NTP reactors.

Exp.	**1** [70]	**2** [74]	**3** [67]	**4** [71]	**5** [77]	**6** [76]	**7** [68]
	Positive DC Corona discharge (pin-plate)	Glass beads packed bed DBD (cylindrical reactor)	DBD (cylindrical reactor)	positive DC Corona (pin-plate)	$BaTiO_3$ packed bed DBD (cylindrical reactor)	DBD (wire-plate)	Positive DC corona discharge (pin-plate)
C_{tol} (ppm_v)	45	240	200	0.5	500	100	0.5
Gap (mm)	9	6	2	20	-	10	-
V_R [1]/mL (tr [2]/s)	72 (4.5 × 10^{-4})	13.2 (2.5)	8.5 (1.7)	250 (1.5)	-	-	250 (1.5)
Exp.	**8** [73]	**9** [69]	**10** [65]	**11** [75]	**12** [66]	**13** [72]	
	DBD (tubular reactor)	Multistage reactor	DBD (tubular reactor)	DBD (tubular reactor)	DBD (tubular reactor)	DBD (tubular reactor)	
C_{tol} (ppm_v)	85	70	800	109	107	107	
Gap (mm)	5.65	-	-	2	2.5	4	
V_R [1]/L (t_r [2]/s)	-	-	-	11.9 (1.4)	14.9 (1.8)	-	

[1] Reactor volume; [2] Residence time.

In order to investigate the benefit of adding a catalytic reactor downstream the NTP, toluene removal efficiency from PPC experiments has been plotted in Figure 8 as a function of toluene removal efficiency from separated NTP experiments. It is remarkable that all the points lie above the bisector showing the beneficial role of integrating a MnO_x-based catalyst downstream the NTP reactor. All the more the points deviate from the bisector; all the more the catalyst plays a beneficial role when integrated in the PPC process all other things being otherwise equal. The most improvement is obtained in Exp.12 with a decreasing beneficial effect, depending on the nature of the catalyst, as follows: Exp.12c > Exp.12b > Exp.12d > Exp.12a. Hence, in this case, a direct comparison of the catalyst performances can be undertaken. It is thus found a beneficial role of integrating Co to Mn in equal amount (Exp.12c). The presence of $Co_3Mn_3O_4$, along with a segregated Co_3O_4 spinel phase, promotes toluene removal efficiency compared to the reference MnO_x solid. Similarly the catalysts in Exp.13 can be ranked by decreasing activity: Exp.13b > Exp.13c > Exp.13a or more clearly: 13b (10 wt % $CoMnO_x$/ZSM-5, Co/Mn = 1) > 13c (10 wt % $CeMnO_x$/ZSM-5, Ce/Mn = 1) > 13a (10 wt % MnO_x/ZSM-5). Thus, good performances for toluene abatement can be obtained over $CoMnO_x$, as bulk or dispersed on the ZMS-5 support. It was claimed that the mixture of $Co_3Mn_3O_4$, MnO_2 and Mn_3O_4 phases in enhancing structural defects significantly promotes the toluene abatement reaction. Likewise, the different catalysts investigated in Exp.2 can be ranked as follows: MnO/AC (Exp.2c) > MnO_2/Al_2O_3 (Exp.2b) > MnO_2-Fe_3O_4 (Exp.2a). This study underlined the important role of the support as the activity of the catalyst depends mainly on the support. When regarding MnO/AC, the low Mn content, the high surface area of the support, the nature of the counter-anion of the Mn precursor (OAc) as well as the conditions of calcination (in N_2 at 300 °C) ensured a good Mn dispersion combined to a low Mn AOS. These two properties are responsible for toluene oxidation into CO_2 in an effective way. A series of CuO/MnO_2 catalysts with different Cu loadings were synthesized by the incipient wetness impregnation method in Exp.10. Higher activity of 10 wt % CuO/MnO_2 can be attributed to a better dispersion of the active phase. However caution must be exercised in the interpretation of these results due to lacking key information such as the $[O_3]/[Toluene]_0$ ratio defined above as well as the CO_2 yield. Additionally, the 100% toluene conversion achieved over Ag–Mn–O (Exp.11) has also to be highlighted but however the high silver content (10 wt %) can be a drawback.

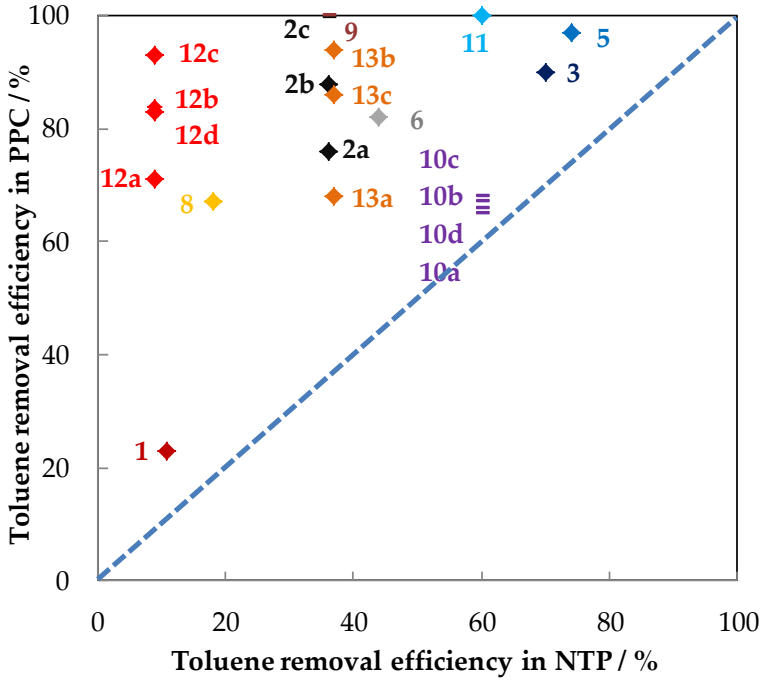

Figure 8. Toluene removal efficiency in PPC as a function of Toluene removal efficiency in NTP reactor.

To achieve a better insight in terms of efficiency of the process, which means the total oxidation of toluene into CO_2 and H_2O, the toluene conversion into CO_2 (CO_2 yield) has been drawn as a function of toluene removal efficiency (see Figure 9). This representation highlights more accurately the efficiency of the PPC process as the toluene removal efficiency takes only account for the amount of toluene removed making no distinction between CO_2 and other possible organic by-products. The representation allows to distinguish two sets of PPC processes: set 1 delimited by the blue circle and set 2 consisting in the remaining ones. The set 1 includes the most efficient PPC configurations 13b, 3a, and 13c, namely (DBD; $CoMnO_x$/ZSM5), (DBD; Mn–P–O, Mn-1), and (DBD; $CeMnO_x$/ZSM5). Set 2 includes the PPC configurations 2c, 9c, 9a, 9b, 2b, 2a and 13a, namely (Glass packed bed DBD; MnO/AC), (multistage DBD; MnO_2-CuO + MnO_2/Aluminum honeycomb), (multistage DBD; MnO_2/Aluminum honeycomb), (multistage DBD; MnO_2-CuO), (Glass packed bed DBD; MnO_2/γ-Al_2O_3), (Glass packed bed DBD; N150 (MnO_2-Fe_2O_3)) and (DBD; MnO_x/ZSM-5). A direct comparison is unfortunately restrictive as it is not possible to get the information in terms in CO_2 yield from numerous papers as in many papers mineralization rate (or CO_x selectivity) is given.

Improving the global efficiency of the PPC process requires that the NTP works at low ED while minimizing the formation of undesirable by-products. CO_2 yield as a function of reactor energy density given shown in Figure 10 emphasizes the efficiency of the $CoMnO_x$/ZSMS-5 (Exp.13b) and $CeMnO_x$/ZSM-5 (Exp.13a) catalysts located downstream of a DBD reactor to convert toluene into CO_2 at low ED. Additionally, as a good performance in terms of CO_2 yield is also achieved with a pulsed DBD reactor in combination with the manganese phosphate catalyst [67] a quite high ED results in an energy yield of 1.84 g/kWh (see below) with a factor of about 2 lower than that of Exp.13 of 4.2 g/kWh.

When considering PPC, the ratio $R = [O_3]_{in}/[Tol]_0$ ($[O_3]$: concentration of ozone injected in the catalytic reactor; $[Tol]_{0:}$ concentration of toluene injected in the NTP reactor) is a key parameter as the O_3 may be in a sufficient amount enabling total mineralization of toluene. Considering the mode of decomposition of O_3 over MnO_x the reaction of toluene abatement by O_3 can be formally written as follows:

$$C_7H_8 + 18O_3 \rightarrow 7CO_2 + 4H_2O + 18O_2 \quad (15)$$

The fundamental assumption is that each O_3 is converted to a single O radical and that toluene is oxidized only by active oxygen species on the surface of the catalyst. However, at low toluene conversion, active oxygen species mainly degrade the plasma non processed toluene while at higher conversion they are mainly implied in the degradation of the gaseous carbonaceous by-products produced in the course of the NTP treatment whose relative distribution is dependent on the nature of the NTP all things being equal.

R has been represented as a function of toluene conversion into CO_2 in Figure 11. Despite the very limited set of values it is observed a clear linear dependence of *R* as a function of toluene conversion into CO_2. This shows the efficiency of these catalysts to decompose ozone when the value of R is higher than 18.

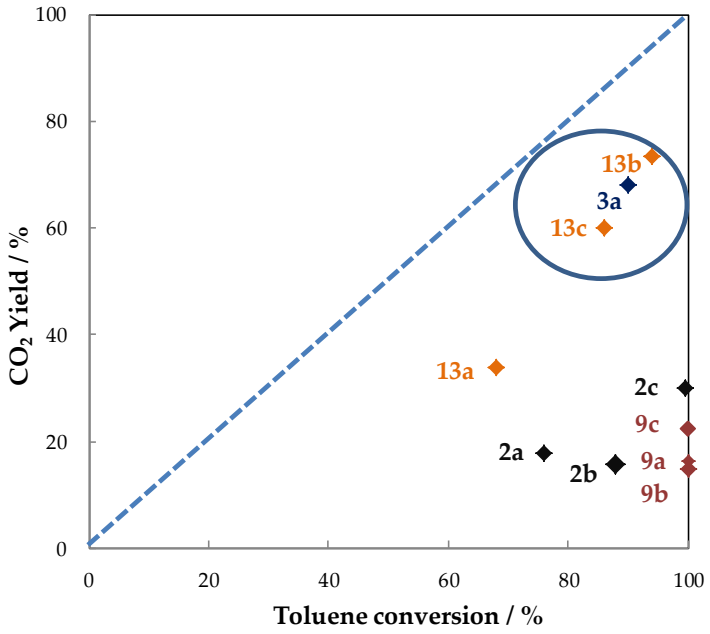

Figure 9. CO_2 yield as a function of Toluene removal efficiency in PPC.

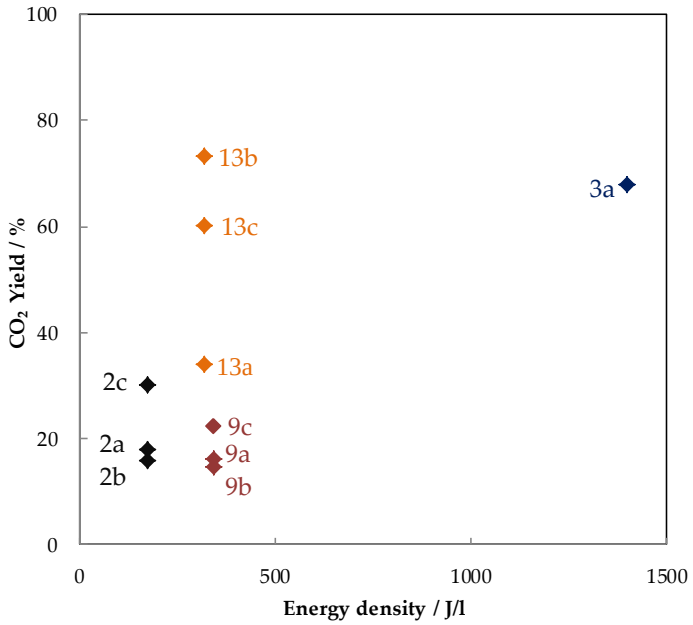

Figure 10. CO_2 yield as a function of energy density in PPC.

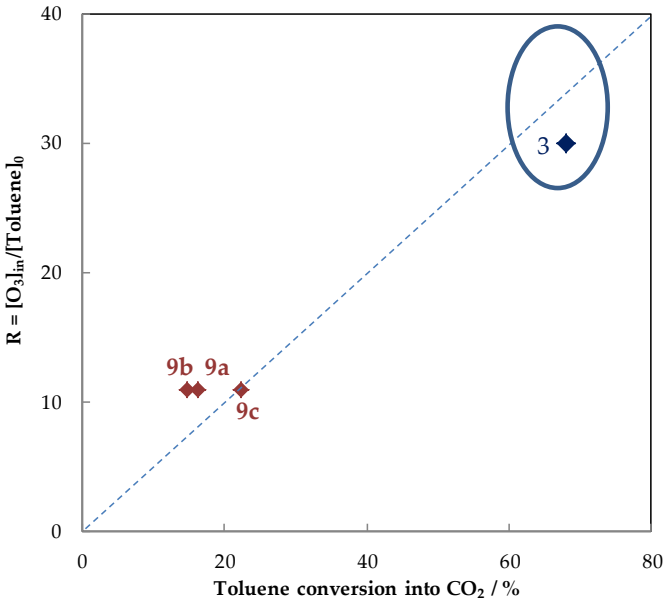

Figure 11. $R = [O_3]_{in}/[Tol]_0$ as a function of CO_2 yield in PPC.

Good performances are obtained with a pulsed dielectric barrier discharge (DBD) at atmospheric pressure and room temperature in combination with manganese phosphate catalyst (Mn-1) placed downstream.

CO and N_2O can be detected as by-products. Benzaldehyde, formic acid, methylbenzoquinone, benzyl alcohol, benzoic acid, and benzyl benzoate constitute some examples of organic by-products which can be identified as intermediates on the surface in the reaction process. These by-products derived from the partial oxidation of toluene. The detection of such ad-species in a strong interaction with the catalyst can cause a decrease in activity of the catalyst in the course of the reaction and leads to a decrease of the carbon mass balance. In the experiments given here no O_3 is detected at the catalytic reactor confirming the efficiency of the catalysts in O_3 decomposition.

The efficiency of the process has also been evaluated in terms of energy yield expressed in grams of toluene removed by kWh (g/kWh). The histogram given in Figure 12 sums up the results. The ranking of PPC configurations in terms of decreasing energy efficiency for the most efficient configurations is: Exp.12 (22–28) ≈ Exp.11 (24) > Exp.2 (14–19) > Exp.8 (11) > Exp.1 (8) > Exp.13 (3–4) ≈ Exp.9 (1.7–3.1). The energy yields can vary from a factor 20 considering all the configurations.

The stability of the Mn oxide-based catalysts in the reactive gaseous mixture over time was investigated in few PPC processes. Durability test carried out for 43 h showed good stability for Ag-Mn–O (Exp.11) [75] in terms of either CO_2 generation, toluene decomposition and ozone degradation. The strong interaction between metallic Ag and Mn_3O_4 was postulated to promote the oxidation of intermediate compounds at room temperature. Durme et al. [71] also reported that no deactivation of the commercial catalyst Cu-Mn/TiO_2 (10 g, 3 wt % Cu, 6.8 wt % MnO_2) was observed for 48 h on stream in PPC configuration at room temperature. The reasons were ascribed to two points. Firstly, no significant amounts of active sites were blocked due to low amount of toluene (0.5 ppmv). Secondly, adsorbed degradation products may also be oxidized efficiently due to high ozone decomposition ability of Cu–Mn/TiO_2. Therefore, the high ozone decomposition ability of metal-MnO_x (e.g., Ag, Cu) can prevent catalyst deactivation.

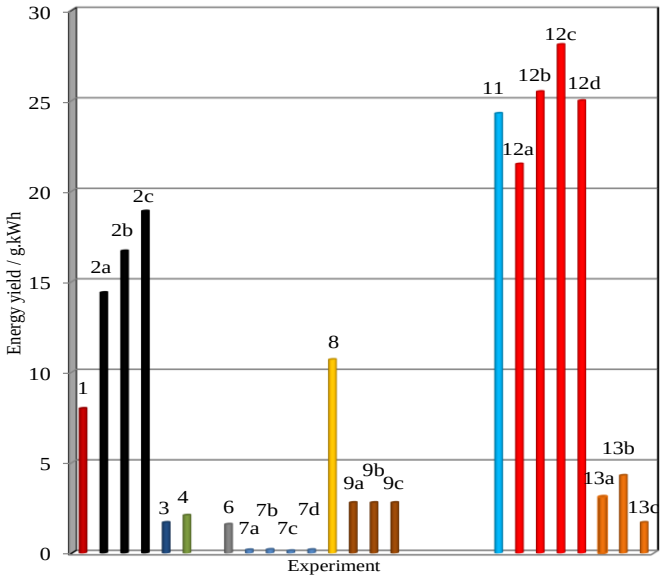

Figure 12. Energy yield as a function of the PPC process.

6. Conclusions and Outlook

The desire to increase the efficiency of toluene depollution processes by reducing their energy consumption while simultaneously reducing toluene emission to meet the more stringent limits has motivated considerable research in advanced toluene oxidation processes. Among them, PPC is a promising method which takes full advantages of the two technologies: high selectivity from catalysis and the easy operation from NTP allowing the hybrid system to work at ambient temperature. A greater CO_2 selectivity can be achieved due to the production of active oxygen produced from plasma generated O_3 catalytic decomposition to remove the by-products. Recent progress in the research on noble metal-free catalysts has highlighted the importance of manganese oxide-based formulations to be involved in such a process. This is because manganese oxides are low-cost, easily synthesized, environmentally friendly and efficient catalysts in ozone decomposition and toluene ozonation.

The best catalytic formulations include Ag–Mn–O, amorphous manganese phosphate, 10 wt % ($CoMnO_x$)/ZSM-5 and MnO/AC. Besides, Co, Ce and Ag are the most efficient additives to promote O_3 decomposition in interaction with manganese oxide. Furthermore, Co allows achieving good performances in moist air, which opens encouraging perspectives. It has to be mentioned that some Ag has to be introduced in the formulation to promote the desorption of organic ad-species and to ensure a good time-on-stream-stability. In terms of energy yields, the PPC configuration of the DBT tubular reactor with Co_3O_4-MnO_2 (Co:Mn = 1:6) catalyst downstream ensures an efficient use of the energy.

Despite the promising improvements resulting from several studies about using related Mn-based oxides active phases, there are still open issues to be addressed regarding the design of the catalyst in order to develop an efficient hybrid process. To improve the efficiency of the catalysts many strategies can be pursued, such as external morphology control, doping, optimization of the active Mn related phase with the nature of the support. Interestingly, the effect of the external morphology of MnO_x which is easily to tune has to be deeply investigated as it may have a significant impact on the density of vacancies, of defects, as well as on the Mn average oxidation state and textural properties of the materials. The role of additives has not been cleared up sufficiently and the effect of other TM oxides has to be investigated in order to minimize CO, NO_x, N_2O and possible O_3 as by-products.

Finally, the stability of the-based Mn oxide catalysts in the reactive gaseous mixture over time has to be investigated more deeply. The carbon balance has to be carried out. Although the beneficial cleaning effect of Ag has been evidenced, the decrease of Ag loading has to be performed while

maintaining satisfactory catalytic performances. In regard the effect of inhibitors such as water as also to be investigated.

Acknowledgments: The joint research program PICS No. 6913 (Preparation of catalysts and catalytic depollution assisted by plasma) from CNRS-FWO (FWO-W0.002.15N), the "DepollutAir" project of the European Program INTERREG V France—Wallonie—Flanders (FEDER), Chevreul institute (FR 2638), Ministère de l'Enseignement Supérieur et de la Recherche and Région Hauts-de-France are acknowledged for supporting and funding this work.

Author Contributions: Zhiping Ye wrote the first draft of the review which was then refined by Jean-Marc Giraudon, and the comments and suggestions by Nathalie De Geyter, Rino Morent and Jean-François Lamonier.

Conflicts of Interest: The authors declare no conflict of interest.

References

1. World Health Organization. *5.14 Toluene*; WHO Regional Office for Europe, Ed.; WHO: Copenhagen, Denmark, 2000.
2. Agency for Toxic Substances and Disease Registry (ATSDR). *Toxicological Profile for Toluene*; U.S. Department of Health and Human Services, U.S. Public Health Service: Atlanta, GA, USA, 2000.
3. World Health Organization. *Environmental Health Criteria 52: Toluene*; World Health Organization: Geneva, Switzerland, 1985.
4. Guo, Y.; Liao, X.; Fu, M.; Huang, H.; Ye, D. Toluene decomposition performance and NOx by-product formation during a DBD-catalyst process. *J. Environ. Sci.* **2015**, *28*, 187–194. [CrossRef] [PubMed]
5. Kim, H.-H.; Teramoto, Y.; Ogata, A.; Takagi, H.; Nanba, T. Plasma catalysis for environmental treatment and energy applications. *Plasma Chem. Plasma Process.* **2016**, *36*, 45–72. [CrossRef]
6. Whitehead, J.C. Plasma–catalysis: The known knowns, the known unknowns and the unknown unknowns. *J. Phys. D Appl. Phys.* **2016**, *49*, 243001. [CrossRef]
7. Furniss, B.S. *Vogel's Textbook of Practical Organic Chemistry*; Longman/Wiley: New York, NY, USA, 1989.
8. Genuino, H.C.; Dharmarathna, S.; Njagi, E.C.; Mei, M.C.; Suib, S.L. Gas-Phase Total Oxidation of Benzene, Toluene, Ethylbenzene, and Xylenes Using Shape-Selective Manganese Oxide and Copper Manganese Oxide Catalysts. *J. Phys. Chem. C* **2012**, *116*, 12066–12078. [CrossRef]
9. Market Study: Toluene. Available online: http://www.ceresana.com/en/market-studies/chemicals/toluene/ (accessed on 13 February 2018).
10. Toluene Uses and Market Data. Available online: http://www.icis.com/resources/news/2007/11/07/9076550/toluene-uses-and-market-data/ (accessed on 13 February 2018).
11. Corporation, T.E. *Locating and Estimating Air Emissions from Soruces of Toluene*; EPA: Chapel Hill, NC, USA, 1994; p. 207.
12. Hobara, T.; Okuda, M.; Gotoh, M.; Oki, K.; Segawa, H.; Kunitsugu, I. Estimation of the lethal toluene concentration from the accidental death of painting workers. *Ind. Health* **2000**, *38*, 228–231. [CrossRef] [PubMed]
13. Lu, B.; Zhang, X.; Yu, X.; Feng, T.; Yao, S. Catalytic oxidation of benzene using DBD corona discharges. *J. Hazard. Mater.* **2006**, *137*, 633–637. [CrossRef] [PubMed]
14. Van Durme, J.; Dewulf, J.; Leys, C.; Van Langenhove, H. Combining non-thermal plasma with heterogeneous catalysis in waste gas treatment: A review. *Appl. Catal. B Environ.* **2008**, *78*, 324–333. [CrossRef]
15. Kim, H.H. Nonthermal plasma processing for air-pollution control: A historical review, current issues, and future prospects. *Plasma Process. Polym.* **2004**, *1*, 91–110. [CrossRef]
16. McAdams, R. Pulsed corona treatment of gases: System scaling and efficiency. *Plasma Sources Sci. Technol.* **2007**, *16*, 703. [CrossRef]
17. Chen, H.L.; Lee, H.M.; Chen, S.H.; Chang, M.B.; Yu, S.J.; Li, S.N. Removal of volatile organic compounds by single-stage and two-stage plasma catalysis systems: A review of the performance enhancement mechanisms, current status, and suitable applications. *Environ. Sci. Technol.* **2009**, *43*, 2216–2227. [CrossRef] [PubMed]
18. Magureanu, M.; Mandache, N.B.; Eloy, P.; Gaigneaux, E.M.; Parvulescu, V.I. Plasma-assisted catalysis for volatile organic compounds abatement. *Appl. Catal. B Environ.* **2005**, *61*, 12–20. [CrossRef]
19. Xiao, G.; Xu, W.; Wu, R.; Ni, M.; Du, C.; Gao, X.; Luo, Z.; Cen, K. Non-thermal plasmas for VOCs abatement. *Plasma Chem. Plasma Process.* **2014**, *34*, 1033–1065. [CrossRef]

20. Kim, H.H.; Prieto, G.; Takashima, K.; Katsura, S.; Mizuno, A. Performance evaluation of discharge plasma process for gaseous pollutant removal. *J. Electrost.* **2002**, *55*, 25–41. [CrossRef]
21. Vandenbroucke, A.M.; Morent, R.; De Geyter, N.; Leys, C. Non-thermal plasmas for non-catalytic and catalytic VOC abatement. *J. Hazard. Mater.* **2011**, *195*, 30–54. [CrossRef] [PubMed]
22. Vandenbroucke, A.M.; Morent, R.; Geyter, N.D.; Leys, C. Decomposition of toluene with plasma-catalysis: A review. *J. Adv. Oxid. Technol.* **2012**, *15*, 232–241. [CrossRef]
23. Tian, Z.-Y.; Mountapmbeme Kouotou, P.; Bahlawane, N.; Tchoua Ngamou, P.H. Synthesis of the catalytically active Mn_3O_4 spinel and its thermal properties. *J. Phys. Chem. C* **2013**, *117*, 6218–6224. [CrossRef]
24. Kitchaev, D.A.; Peng, H.; Liu, Y.; Sun, J.; Perdew, J.P.; Ceder, G. Energetics of MnO_2 polymorphs in density functional theory. *Phys. Rev. B* **2016**, *93*, 045132. [CrossRef]
25. Menezes, P.W.; Indra, A.; Littlewood, P.; Schwarze, M.; Göbel, C.; Schomäcker, R.; Driess, M. Nanostructured manganese oxides as highly active water oxidation catalysts: A boost from manganese precursor chemistry. *ChemSusChem* **2014**, *7*, 2202–2211. [CrossRef] [PubMed]
26. Craciun, R.; Nentwick, B.; Hadjiivanov, K.; Knözinger, H. Structure and redox properties of MnOx/Yttrium-stabilized zirconia (YSZ) catalyst and its used in CO and CH_4 oxidation. *Appl. Catal. A Gen.* **2003**, *243*, 67–79. [CrossRef]
27. Kim, S.C.; Shim, W.G. Catalytic combustion of VOCs over a series of manganese oxide catalysts. *Appl. Catal. B Environ.* **2010**, *98*, 180–185. [CrossRef]
28. Li, X.; Xu, J.; Wang, F.; Gao, J.; Zhou, L.; Yang, G. Direct oxidation of toluene to benzoic acid with molecular oxygen over manganese oxides. *Catal. Lett.* **2006**, *108*, 137–140. [CrossRef]
29. Liu, Y.; Dai, H.; Deng, J.; Zhang, L.; Zhao, Z.; Li, X.; Wang, Y.; Xie, S.; Yang, H.; Guo, G. Controlled generation of uniform spherical $LaMnO_3$, $LaCoO_3$, Mn_2O_3, and Co_3O_4 nanoparticles and their high catalytic performance for carbon monoxide and toluene oxidation. *Inorg. Chem.* **2013**, *52*, 8665–8676. [CrossRef] [PubMed]
30. Deng, J.; He, S.; Xie, S.; Yang, H.; Liu, Y.; Guo, G.; Dai, H. Ultralow loading of silver nanoparticles on Mn_2O_3 nanowires derived with molten salts: A high-efficiency catalyst for the oxidative removal of toluene. *Environ. Sci. Technol.* **2015**, *49*, 11089–11095. [CrossRef] [PubMed]
31. Wang, F.; Dai, H.; Deng, J.; Bai, G.; Ji, K.; Liu, Y. Manganese oxides with rod-, wire-, tube-, and flower-like morphologies: Highly effective catalysts for the removal of toluene. *Environ. Sci. Technol.* **2012**, *46*, 4034–4041. [CrossRef] [PubMed]
32. Lahousse, C.; Bernier, A.; Grange, P.; Delmon, B.; Papaefthimiou, P.; Ioannides, T.; Verykios, X. Evaluation of γ-MnO_2 as a VOC removal catalyst: Comparison with a noble metal catalyst. *J. Catal.* **1998**, *178*, 214–225. [CrossRef]
33. Si, W.; Wang, Y.; Peng, Y.; Li, X.; Li, K.; Li, J. A high-efficiency γ-MnO_2-like catalyst in toluene combustion. *Chem. Commun.* **2015**, *51*, 14977–14980. [CrossRef] [PubMed]
34. Liao, Y.; Zhang, X.; Peng, R.; Zhao, M.; Ye, D. Catalytic properties of manganese oxide polyhedra with hollow and solid morphologies in toluene removal. *Appl. Surf. Sci.* **2017**, *405*, 20–28. [CrossRef]
35. Herbschleb, C.T. *ReactorSTM: Imaging Catalysts under Realistic Conditions*; Faculty of Science, Leiden University: Leiden, The Netherlands, 2011.
36. Aguero, F.N.; Scian, A.; Barbero, B.P.; Cadús, L.E. Influence of the support treatment on the behavior of MnO_x/Al_2O_3 catalysts used in VOC combustion. *Catal. Lett.* **2009**, *128*, 268. [CrossRef]
37. Védrine, J.C.; Fechete, I. Heterogeneous partial oxidation catalysis on metal oxides. *C. R. Chim.* **2016**, *19*, 1203–1225. [CrossRef]
38. Imamura, S.; Ikebata, M.; Ito, T.; Ogita, T. Decomposition of ozone on a silver catalyst. *Ind. Eng. Chem. Res.* **1991**, *30*, 217–221. [CrossRef]
39. Dhandapani, B.; Oyama, S.T. Gas phase ozone decomposition catalysts. *Appl. Catal. B Environ.* **1997**, *11*, 129–166. [CrossRef]
40. Li, W.; Gibbs, G.; Oyama, S.T. Mechanism of ozone decomposition on a manganese oxide catalyst. 1. In situ Raman spectroscopy and ab initio molecular orbital calculations. *J. Am. Chem. Soc.* **1998**, *120*, 9041–9046. [CrossRef]
41. Li, W.; Oyama, S.T. Mechanism of ozone decomposition on a manganese oxide catalyst. 2. Steady-state and transient kinetic studies. *J. Am. Chem. Soc.* **1998**, *120*, 9047–9052. [CrossRef]

42. Einaga, H.; Harada, M.; Futamura, S. Structural changes in alumina-supported manganese oxides during ozone decomposition. *Chem. Phys. Lett.* **2005**, *408*, 377–380. [CrossRef]
43. Radhakrishnan, R.; Oyama, S.T.; Ohminami, Y.; Asakura, K. Structure of MnO_x/Al_2O_3 catalyst: A study using EXAFS, in situ laser Raman spectroscopy and ab initio calculations. *J. Phys. Chem. B* **2001**, *105*, 9067–9070. [CrossRef]
44. Jia, J.; Zhang, P.; Chen, L. Catalytic decomposition of gaseous ozone over manganese dioxides with different crystal structures. *Appl. Catal. B Environ.* **2016**, *189*, 210–218. [CrossRef]
45. Kameya, T.; Urano, K. Catalytic decomposition of ozone gas by a Pd impregnated MnO_2 catalyst. *J. Environ. Eng.* **2002**, *128*, 286–292. [CrossRef]
46. Ma, J.; Wang, C.; He, H. Transition metal doped cryptomelane-type manganese oxide catalysts for ozone decomposition. *Appl. Catal. B Environ.* **2017**, *201*, 503–510. [CrossRef]
47. Radhakrishnan, R.; Oyama, S.T.; Chen, J.G.; Asakura, K. Electron transfer effects in ozone decomposition on supported manganese oxide. *J. Phys. Chem. B* **2001**, *105*, 4245–4253. [CrossRef]
48. Setvín, M.; Aschauer, U.; Scheiber, P.; Li, Y.-F.; Hou, W.; Schmid, M.; Selloni, A.; Diebold, U. Reaction of O_2 with subsurface oxygen vacancies on TiO_2 anatase (101). *Science* **2013**, *341*, 988–991. [CrossRef] [PubMed]
49. Rezaei, E.; Soltan, J.; Chen, N. Catalytic oxidation of toluene by ozone over alumina supported manganese oxides: Effect of catalyst loading. *Appl. Catal. B Environ.* **2013**, *136*, 239–247. [CrossRef]
50. Rezaei, E.; Soltan, J. EXAFS and kinetic study of MnO_x/γ-alumina in gas phase catalytic oxidation of toluene by ozone. *Appl. Catal. B Environ.* **2014**, *148*, 70–79. [CrossRef]
51. Rezaei, E.; Soltan, J. Low temperature oxidation of toluene by ozone over MnOx/γ-alumina and MnOx/MCM-41 catalysts. *Chem. Eng. J.* **2012**, *198*, 482–490. [CrossRef]
52. Hu, M.; Hui, K.; Hui, K. Role of graphene in MnO_2/graphene composite for catalytic ozonation of gaseous toluene. *Chem. Eng. J.* **2014**, *254*, 237–244. [CrossRef]
53. Li, J.; Na, H.; Zeng, X.; Zhu, T.; Liu, Z. In situ DRIFTS investigation for the oxidation of toluene by ozone over Mn/HZSM-5, Ag/HZSM-5 and Mn–Ag/HZSM-5 catalysts. *Appl. Surf. Sci.* **2014**, *311*, 690–696. [CrossRef]
54. Sekiguchi, K.; Kurita, Y.; Sankoda, K.; Namiki, N.; Yasui, F.; Tamura, H. Ozone Catalytic Oxidation of Gaseous Toluene over MnO_2-Based Ozone Decomposition Catalysts Immobilized on a Nonwoven Fabric. *Aerosol Air Qual. Res.* **2017**, *17*, 2110–2118. [CrossRef]
55. Liping, L.; Jianguo, Z.; Lixian, Y.; Mingli, F.; Junliang, W.; Huang, B.; Daiqi, Y. Room temperature catalytic ozonation of toluene over MnO_2/Al_2O_3. *Chin. J. Catal.* **2011**, *32*, 904–916.
56. Ramesh, K.; Chen, L.; Chen, F.; Liu, Y.; Wang, Z.; Han, Y.-F. Re-investigating the CO oxidation mechanism over unsupported MnO, Mn_2O_3 and MnO_2 catalysts. *Catal. Today* **2008**, *131*, 477–482. [CrossRef]
57. Royer, S.; Duprez, D. Catalytic oxidation of carbon monoxide over transition metal oxides. *ChemCatChem* **2011**, *3*, 24–65. [CrossRef]
58. Wang, L.-C.; Liu, Q.; Huang, X.-S.; Liu, Y.-M.; Cao, Y.; Fan, K.-N. Gold nanoparticles supported on manganese oxides for low-temperature CO oxidation. *Appl. Catal. B Environ.* **2009**, *88*, 204–212. [CrossRef]
59. Imamura, S.; Tsuji, Y.; Miyake, Y.; Ito, T. Cooperative action of palladium and manganese (III) oxide in the oxidation of carbon monoxide. *J. Catal.* **1995**, *151*, 279–284. [CrossRef]
60. Liang, S.; Teng, F.; Bulgan, G.; Zong, R.; Zhu, Y. Effect of phase structure of MnO_2 nanorod catalyst on the activity for CO oxidation. *J. Phys. Chem. C* **2008**, *112*, 5307–5315. [CrossRef]
61. Wang, X.; Li, Y. Selected-control hydrothermal synthesis of α-and β-MnO_2 single crystal nanowires. *J. Am. Chem. Soc.* **2002**, *124*, 2880–2881. [CrossRef] [PubMed]
62. Wang, X.; Li, Y. Synthesis and formation mechanism of manganese dioxide nanowires/nanorods. *Chemistry* **2003**, *9*, 300–306. [CrossRef] [PubMed]
63. Iablokov, V.; Frey, K.; Geszti, O.; Kruse, N. High catalytic activity in CO oxidation over MnO_x nanocrystals. *Catal. Lett.* **2010**, *134*, 210–216. [CrossRef]
64. Gervasini, A.; Vezzoli, G.; Ragaini, V. VOC removal by synergic effect of combustion catalyst and ozone. *Catal. Today* **1996**, *29*, 449–455. [CrossRef]
65. Quoc An, H.T.; Huu, T.P.; Le Van, T.; Cormier, J.M.; Khacef, A. Application of atmospheric non thermal plasma-catalysis hybrid system for air pollution control: Toluene removal. *Catal. Today* **2011**, *176*, 474–477. [CrossRef]
66. Ye, L.; Feng, F.; Liu, J.; Tang, X.; Zhang, X.; Huang, Y.; Liu, Z.; Yan, K. Toluene decomposition by a two-stage hybrid plasma catalyst system in dry air. *IEEE Trans. Plasma Sci.* **2014**, *42*, 3529–3538. [CrossRef]

67. Magureanu, M.; Mandache, N.; Gaigneaux, E.; Paun, C.; Parvulescu, V. Toluene oxidation in a plasma-catalytic system. *J. Appl. Phys.* **2006**, *99*, 123301. [CrossRef]
68. Van Durme, J.; Dewulf, J.; Demeestere, K.; Leys, C.; Van Langenhove, H. Post-plasma catalytic technology for the removal of toluene from indoor air: Effect of humidity. *Appl. Catal. B Environ.* **2009**, *87*, 78–83. [CrossRef]
69. Harling, A.M.; Glover, D.J.; Whitehead, J.C.; Zhang, K. The role of ozone in the plasma-catalytic destruction of environmental pollutants. *Appl. Catal. B Environ.* **2009**, *90*, 157–161. [CrossRef]
70. Grossmannova, H.; Neirynck, D.; Leys, C. Atmospheric discharge combined with Cu-Mn/Al_2O_3 catalyst unit for the removal of toluene. *Czechoslov. J. Phys.* **2006**, *56*, B1156–B1161. [CrossRef]
71. Van Durme, J.; Dewulf, J.; Sysmans, W.; Leys, C.; Van Langenhove, H. Efficient toluene abatement in indoor air by a plasma catalytic hybrid system. *Appl. Catal. B Environ.* **2007**, *74*, 161–169. [CrossRef]
72. Huang, Y.; Dai, S.; Feng, F.; Zhang, X.; Liu, Z.; Yan, K. A comparison study of toluene removal by two-stage DBD-catalyst systems loading with MnO_x, $CeMnO_x$, and $CoMnO_x$. *Environ. Sci. Pollut. Res.* **2015**, *22*, 19240–19250. [CrossRef] [PubMed]
73. Hayashi, K.; Yasui, H.; Tanaka, M.; Futamura, S.; Kurita, S.; Aoyagi, K. Temperature dependence of toluene decomposition behavior in the discharge–catalyst hybrid reactor. *IEEE Trans. Ind. Appl.* **2009**, *45*, 1553–1558. [CrossRef]
74. Delagrange, S.; Pinard, L.; Tatibouët, J.-M. Combination of a non-thermal plasma and a catalyst for toluene removal from air: Manganese-based oxide catalysts. *Appl. Catal. B Environ.* **2006**, *68*, 92–98. [CrossRef]
75. Tang, X.; Feng, F.; Ye, L.; Zhang, X.; Huang, Y.; Liu, Z.; Yan, K. Removal of dilute VOCs in air by post-plasma catalysis over Ag-based composite oxide catalysts. *Catal. Today* **2013**, *211*, 39–43. [CrossRef]
76. Huang, H.; Ye, D.; Guan, X. The simultaneous catalytic removal of VOCs and O_3 in a post-plasma. *Catal. Today* **2008**, *139*, 43–48. [CrossRef]
77. Demidyuk, V.; Whitehead, J.C. Influence of temperature on gas-phase toluene decomposition in plasma-catalytic system. *Plasma Chem. Plasma Process.* **2007**, *27*, 85–94. [CrossRef]
78. Chlala, D.; Giraudon, J.-M.; Nuns, N.; Lancelot, C.; Vannier, R.-N.; Labaki, M.; Lamonier, J.-F. Active Mn species well dispersed on Ca^{2+} enriched apatite for total oxidation of toluene. *Appl. Catal. B Environ.* **2016**, *184*, 87–95. [CrossRef]
79. Spasova, I.; Nikolov, P.; Mehandjiev, D. Ozone decomposition over alumina-supported copper, manganese and copper-manganese catalysts. *Ozone* **2007**, *29*, 41–45. [CrossRef]
80. Vepřek, S.; Cocke, D.; Kehl, S.; Oswald, H. Mechanism of the deactivation of Hopcalite catalysts studied by XPS, ISS, and other techniques. *J. Catal.* **1986**, *100*, 250–263. [CrossRef]
81. Puckhaber, L.S.; Cheung, H.; Cocke, D.L.; Clearfield, A. Reactivity of copper manganese oxides. *Solid State Ion.* **1989**, *32*, 206–213. [CrossRef]
82. Li, W.; Zhuang, M.; Wang, J. Catalytic combustion of toluene on Cu-Mn/MCM-41 catalysts: Influence of calcination temperature and operating conditions on the catalytic activity. *Catal. Today* **2008**, *137*, 340–344. [CrossRef]
83. Li, X.; Wang, L.; Xia, Q.; Liu, Z.; Li, Z. Catalytic oxidation of toluene over copper and manganese-based catalysts: Effect of water vapor. *Catal. Commun.* **2011**, *14*, 15–19. [CrossRef]
84. Aguilera, D.A.; Perez, A.; Molina, R.; Moreno, S. Cu–Mn and Co.–Mn catalysts synthesized from hydrotalcites and their use in the oxidation of VOCs. *Appl. Catal. B Environ.* **2011**, *104*, 144–150. [CrossRef]
85. Li, W.; Zhuang, M.; Xiao, T.; Green, M. MCM-41 supported Cu–Mn catalysts for catalytic oxidation of toluene at low temperatures. *J. Phys. Chem. B* **2006**, *110*, 21568–21571. [CrossRef] [PubMed]
86. Behar, S.; Gonzalez, P.; Agulhon, P.; Quignard, F.; Świerczyński, D. New synthesis of nanosized Cu–Mn spinels as efficient oxidation catalysts. *Catal. Today* **2012**, *189*, 35–41. [CrossRef]
87. Saqer, S.M.; Kondarides, D.I.; Verykios, X.E. Catalytic oxidation of toluene over binary mixtures of copper, manganese and cerium oxides supported on γ-Al_2O_3. *Appl. Catal. B Environ.* **2011**, *103*, 275–286. [CrossRef]
88. Zimowska, M.; Michalik-Zym, A.; Janik, R.; Machej, T.; Gurgul, J.; Socha, R.; Podobiński, J.; Serwicka, E. Catalytic combustion of toluene over mixed Cu–Mn oxides. *Catal. Today* **2007**, *119*, 321–326. [CrossRef]
89. Ye, Z.; Giraudon, J.-M.; Nuns, N.; Simon, P.; De Geyter, N.; Morent, R.; Lamonier, J.-F. Influence of the preparation method on the activity of copper-manganese oxides for toluene total oxidation. *Appl. Catal. B Environ.* **2018**, *223*, 154–166. [CrossRef]
90. Lian, Z.; Ma, J.; He, H. Decomposition of high-level ozone under high humidity over Mn–Fe catalyst: The influence of iron precursors. *Catal. Commun.* **2015**, *59*, 156–160. [CrossRef]

91. Khacef, A.; Huu, T.P.; An, H.T.Q.; Le Van, T.; Cormier, J.-M. Removal of Toluene in Air by Non Thermal Plasma-Catalysis Hybrid System. In Proceedings of the 20th International Symposium of Plasma Chemistry, Philadelphia, PA, USA, 24–29 July 2011; pp. 1–4.
92. Konelschatz, U.; Eliasson, B.; Egli, W. Dielectric-Barrier Discharges. Principle and Applications. *J. Phys. IV Colloq.* **1997**, *7*, C4-47.
93. Chang, J.; Kostov, K.; Urashima, K.; Yamamoto, T.; Okayasu, Y.; Kato, T.; Iwaizumi, T.; Yoshimura, K. Removal of NF_3 from semiconductor process flue gases by tandem packed bed plasma-adsorbent hybrid systems. In Proceedings of the 1998 IEEE Industry Applications Conference. Thirty-Third IAS Annual Meeting, St. Louis, MO, USA, 12–15 October 1998; IEEE: Piscataway, NJ, USA, 1998; pp. 1845–1852.
94. Veerapandian, S.K.; Leys, C.; De Geyter, N.; Morent, R. Abatement of VOCs Using Packed Bed Non-Thermal Plasma Reactors: A Review. *Catalysts* **2017**, *7*, 113. [CrossRef]